Computational modelling of cambium activity provides a regulatory framework for simulating radial plant growth

Ivan Lebovka[1], Bruno Hay Mele[5,7], Xiaomin Liu[1], Alexandra Zakieva[1], Theresa Schlamp[1], Nial Gursanscky[2], Roeland M.H. Merks[3,4], Ruth Großeholz[1,6]*, Thomas Greb[1]*

[1]Centre for Organismal Studies, Heidelberg University, Im Neuenheimer Feld 360, Heidelberg, Germany

[2]Gregor Mendel Institute, Vienna Biocenter, Dr. Bohr-Gasse 3, 1030 Vienna, Austria

[3]Mathematical Institute, University Leiden, P.O. Box 9512, 2300 RA, Leiden, The Netherlands

[4]Institute of Biology, Leiden University, P.O. Box 9505, 2300 RA, Leiden, The Netherlands

[5]Department of Agricultural Sciences, Università degli Studi di Napoli Federico II - Reggia di Portici - Via Università, 100 - 80055 - Portici (NA), Italy

[6]BioQuant, Heidelberg University, Im Neuenheimer Feld 267, Heidelberg, Germany

[7]present address: Department of Biology, University of Naples Federico II, Via Cinthia, 26 80126 Naples (NA), Italy

Keywords: cambium, radial plant growth, PXY, CLE41, cellular model, VirtualLeaf

*Corresponding authors, contact:

Thomas Greb, Im Neuenheimer Feld 360, 69120 Heidelberg, phone +49-6221-545524, fax +49-6221-54 6424, thomas.greb@cos.uni-heidelberg.de

23 Ruth Großeholz, Im Neuenheimer Feld 267, 69120 Heidelberg, phone +49-6221-
24 5451276, fax +49-6221-5451483, ruth.grosseholz@bioquant.uni-heidelberg.de

Abstract

Precise organization of growing structures is a fundamental process in developmental biology. In plants, radial growth is mediated by the cambium, a stem cell niche continuously producing wood (xylem) and bast (phloem) in a strictly bidirectional manner. While this process contributes large parts to terrestrial biomass, cambium dynamics eludes direct experimental access due to obstacles in live cell imaging. Here, we present a cell-based computational model visualizing cambium activity and integrating the function of central cambium regulators. Performing iterative comparisons of plant and model anatomies, we conclude that the receptor-like kinase PXY and its ligand CLE41 are part of a minimal framework sufficient for instructing tissue organization. By integrating tissue-specific cell wall stiffness values, we moreover probe the influence of physical constraints on tissue geometry. Our model highlights the role of intercellular communication within the cambium and shows that a limited number of factors is sufficient to create radial growth by bidirectional tissue production.

Impact statement

Radial plant growth produces large parts of terrestrial biomass and can be computationally simulated with the help of an instructive framework of intercellular communication loops.

Introduction

Stem cells in plants are crucial for their longevity and usually maintained in meristems, special cellular environments constituting protective niches [1]. At key positions in the plant body, we find distinct types of meristems that maintain their activity throughout a plant's life cycle. Shoot and root apical meristems (SAM, RAM) are located at the tips of shoots and roots, respectively, driving longitudinal growth and the formation of primary tissue anatomy in these organs. Moreover, lateral meristems organized in cylindrical domains at the periphery of shoots and roots execute their thickening. The cambium is the most prominent among these lateral meristems [2]. Cambium cells are embedded in two distinct vascular tissues produced in opposite directions by periclinal cell divisions: xylem (wood) and phloem (bast) [3, 4]. These tissues carry out fundamental physiological functions: long-distance transport of water and nutrients in case of the xylem and translocation of sugars and a multitude of signaling molecules in the case of the phloem. Based on its tightly controlled bidirectionality of tissue production and resulting bipartite organization, the cambium is a paradigm for bifacial stem cell niches which produce two tissue types in opposite directions and are found across different kingdoms of life [5].

Balancing proliferation and differentiation within meristems is essential. In the SAM and the RAM this balance is maintained via interaction between the pool of stem cells and the organizing center (OC) and the quiescent center (QC), respectively, where the rate of cell division is relatively low. Both domains form a niche within the meristem instructing surrounding stem cells via regulatory feedback loops [6-10]. In comparison to apical meristems, functional characterization of cambium domains was

performed only very recently. During their transition from stem cells to fully differentiated xylem cells, early xylem cells instruct radial patterning of the cambium including stem cell activity and, thus, similar to the OC in the SAM, fulfil this role only transiently [11]. In addition to influence from the early xylem, phloem-derived DNA-BINDING ONE ZINC FINGER (DOF) transcription factors designated as PHLOEM EARLY DOFs (PEARs) move to cambium stem cells and stimulate their proliferation in a non-cell autonomous manner [12]. Furthermore, genetically encoded lineage tracing experiments showed that cell divisions are mostly restricted to individual bifacial stem cells located in the central cambium feeding both xylem and phloem production [11, 13, 14]. Altogether these findings defined functional cambium domains and revealed some of their reciprocal communication.

Another central and well-established mechanism regulating cambium activity in the reference plant *Arabidopsis thaliana* and beyond [15-18] is the action of a receptor-ligand pair formed by the plasma membrane-bound receptor-like kinase PHLOEM INTERCALATED WITH XYLEM (PXY), also known as TDIF RECEPTOR (TDR), and the secreted CLAVATA3/ESR-RELATED 41 (CLE41) and CLE44 peptides. Like the PEAR proteins [12], CLE41 and CLE44 are expressed in the phloem and thought to diffuse to dividing cells in the cambium area expressing PXY [16, 19]. Direct binding of CLE41 to PXY [19-21] promotes the expression of the transcription factor WUSCHEL RELATED HOMEOBOX 4 (WOX4) [22], which, in turn, is crucial for maintaining the capacity of cells to proliferate [15, 22, 23]. At the same time, the PXY/CLE41 module is reported to repress xylem differentiation in a *WOX4*-independent manner [22, 24]. In this context, PXY stimulates the activity of glycogen synthase kinase 3 proteins (GSK3s), like BRASSINOSTEROID-INSENSITIVE 2

(BIN2) [24]. BIN2, in turn, represses the transcriptional regulator BRI1-EMS SUPPRESSOR 1 (BES1), which mediates brassinosteroid (BR) signaling and promotes xylem differentiation [24, 25]. In line with the hypothesis of a dual role in regulating stem cell activity and xylem differentiation, *PXY* is expressed in the proximal cambium zone containing developing xylem cells and in the central cambium zone containing bifacial cambium stem cells [13, 26, 27].

Distally to the *PXY* expression domain and oriented toward the phloem, the closest homolog to PXY, the receptor-like kinase MORE LATERAL GROWTH 1 (MOL1), represses cambium activity [28, 29]. Although their extracellular domains are highly similar, *PXY* and *MOL1* cannot functionally replace each other, indicating that MOL1 activity does not depend on CLE41/44 peptides and that distinct signaling loops act in the proximal and distal cambium domains [29]. The latter conclusion is supported by the finding that the AUXIN RESPONSE FACTOR5 (ARF5) is expressed in the proximal cambium and promotes the transition from stem cells to xylem cells by directly dampening *WOX4* activity [26, 30]. ARF5 activity is enhanced by phosphorylation through the GSK3 BIN2-LIKE 1 (BIL1) which, in contrast to other GSK3s [24], is inhibited by the PXY/CLE41 module [30].

As the role of multiple communication cascades between different cambium-related tissues is beginning to emerge, it is vital to generate a systemic view on their combined impact on cambium activity and patterning integrated into a dynamic tissue environment. However, although the cambium plays an instructive role for stem cell biology, a dynamic view on its activity is missing due to its inaccessibility for live cell imaging. Computational modeling, in particular agent-based modeling combining

tissue layout with biochemical signaling processes, can overcome these obstacles and help analyzing the interplay between cellular signaling processes, cell growth and cell differentiation *in silico* that would otherwise be inaccessible. Here, we present a dynamic, agent-based computational model [31] of the cambium integrating the functions of PXY, CLE41, and putative phloem-derived signals into a plant-specific modelling framework. As revealed by informative cambium markers, our model is able to reproduce anatomical features of the cambium in a dynamic manner. It also allows studying the cambium as a flexible system comprised of multiple interacting factors, and the effects of those factors on cell division, differentiation and tissue patterning.

Results

Establishing a dynamic cambium model

Taking advantage of the almost exclusive radial expansion of mature plant growth axes, we sought to create a minimal framework recapitulating the 2D dynamics of radial plant growth. To do so, we first produced a simplified stereotypic 2D-representation of a plant growth axis displaying a secondary anatomy by employing VirtualLeaf – a framework specially designed for agent-based modeling of plant tissue growth [32, 33]. To avoid confusion, we refer to factors within the model by an asterisk: e.g., GENE – refers to the plant gene, whereas GENE* refers to its model counterpart. Within the model we defined three cell types: Cells designated as cambium*, cells present in the center referred to as xylem*, and cells present distally to the cambium* designated as phloem* (Figure 1A). These cell* types were organized in concentric domains as observed after the establishment of a secondary organ anatomy [11]. To reduce the risk of losing cambium cells* during our simulations and allow differential cambium cell* behavior right from the start, we defined a rather large starting pool of cambium cells*. We then defined rules determining cell* behavior: **i)** all cells* grew until they reached a size specific for each cell* type, **ii)** cambium cells* divided when they exceeded a certain size, **iii)** cambium cells* changed their identity into xylem* or phloem* depending on the conditions described below (see also supporting information, Supplementary File 1). All chemical-like factors* implemented in the model had manually chosen cell* type-specific production and degradation rates.

To implement context-dependent regulation of cambial cell division and differentiation, we took advantage of the PXY/CLE41 signaling module [19, 22]: Phloem cells* produced a factor designated as CLE41* able to diffuse between cells*, whereas the corresponding, non-diffusing receptor designated as PXY* is produced in cambium cells* (Figure 1B). Recapitulating the CLE41-dependent function of PXY, we considered the following reaction:

$$CLE41^* + PXY^* \rightarrow PXY^*_{active} \quad (1)$$

Thereby, the presence of both CLE41* and PXY* in a cell turned PXY* into PXY_{active}* (Figure 1B). For cambium cells* we described the PXY*-CLE41* interaction by the following equations:

$$\frac{d}{dt}[PXY^*_{active}] = [PXY^*] \cdot [CLE41^*] - degradation_{PXY^*_{active}} \cdot [PXY^*_{active}] \quad (2)$$

$$\frac{d}{dt}[PXY^*] = \frac{production_{PXY}}{(1+suppress\ rate \cdot [PXY^*_{active}])} - [PXY^*] \cdot [CLE41^*] - degradation_{PXY} \cdot [PXY^*] \quad (3)$$

$$\frac{d}{dt}[CLE41^*] = diffusion_{CLE41} - [PXY^*] \cdot [CLE41^*] - degradation_{CLE41} \cdot [CLE41^*] \quad (4)$$

In these equations, [X*] denoted the concentration of the respective factor in each cell*. Since PXY-CLE41 signaling was reported to negatively regulate *PXY* expression [16], we assumed that the production rate of PXY* is inhibited by [PXY_{active}*]. Therefore, the higher [PXY_{active}*] in a given cell*, the less PXY* was produced (equation 3). To integrate PXY/CLE41-dependent regulation of cell proliferation, we let cambium cells* divide only when [PXY_{active}*] exceeded a certain threshold. Thereby, the proliferation of cambium cells* was dependent on both, locally produced PXY* and CLE41* originating from the phloem*. To instruct the differentiation of cambium cells*, we took advantage of the observation that the

PXY/CLE41 module represses xylem differentiation [19, 24]. Consequently, we instructed cambium cells* to change their identity into xylem* as soon as they reached a certain size and [PXY_{active}*] became lower than a threshold value (Supplementary file 1).

In the resulting Model 1, the growing structure maintained a circular pool of dividing cambium cells* with a high concentration of PXY_{active}* while producing xylem cells* toward the center of the organ (Figure 1C, Video 1, Video 2, Video 3, Video 4). As expected, when cambium cells* were displaced to the proximal side of the cambium*, they stopped dividing likely due to low [PXY_{active}*] (Figure 1C, D, Video 3, Video 4, Video 5) allowing them to reach a size sufficient for xylem* differentiation. Cell* division rates were highest close to CLE41* producing phloem cells* (Figure 1D-G, Video 2, Video 3). Moreover, as PXY_{active}* negatively affected the production of PXY*, [PXY*] was particularly low in the distal cambium* region (Figure 1C, F, G. Video 1, Video 5). This pattern was reminiscent of the exclusive activity of the *PXY* promoter in the proximal cambium area observed previously [13, 29]. Thus, although phloem was not produced, with maintaining a circular domain of cambium cells* and cell* proliferation and with promoting xylem* production, Model 1 was able to recapitulate several core features of the active cambium.

The combination of *PXY* and *SMXL5* promoter reporters reveals cambium anatomy

To identify rules for phloem formation, we took advantage of findings obtained using the *PXYpro:CYAN FLUORESCENT PROTEIN* (*PXYpro:CFP*) and *SUPPRESSOR*

OF MAX2-LIKE 5pro:YELLOW FLUORESCENT PROTEIN (*SMXL5pro:YFP*) markers, recently established read-outs for cambium anatomy [13]. *PXYpro:CFP* and *SMXL5pro:YFP* markers label the proximal and distal cambium domain (Figure 2A, Figure 2—figure supplement 1), respectively, and are therefore indicative of a bipartite cambium organization. *PXYpro:CFP* activity indicates the proximal xylem formation zone whereas *SMXL5pro:YFP* activity indicates the distal phloem formation zone. A narrow central zone in which both markers are active hold cambium stem cells which feed both tissues and also show a high rate of cell divisions in comparison to xylem and phloem progenitors [13].

To computationally recapitulate the observed maximum of cell division rates in the central cambium domain, we sought to inhibit cell* divisions in the distal layers of the cambium*. Such an effect is, for instance, mediated by the receptor-like kinase MOL1, which, similarly to *SMXL5*, is expressed distally to *PXY* expressing cells and suppresses cambial cell divisions [29]. Because cells* in the distal cambium* region were characterized by high levels of PXY_{active}* (Figure 1C, G, Video 4), we used PXY_{active}* to locally inhibit cell* division and, at the same time, to instruct phloem* formation. Therefore, we modified the rule for cell* differentiation such that, when a cambium cell* reached a specific size, it differentiated into xylem* if [PXY_{active}*] became lower than a threshold value and into phloem* if [PXY_{active}*] was greater than the same threshold and the cell was larger (Supplementary File 1). Thereby, our model followed a classical ‘French flag’ principle of development according to which concentration gradients of diffusible morphogens pattern surrounding tissues [34]. It is worth noting that the combined effect of CLE41* on cell* proliferation, on phloem*

224 specification and on [PXY*] may also be achieved by distinct phloem-derived factors
225 mediating these effects individually.

226

227 The computational implementation of these rules (Model 2A) resulted in a
228 descending gradient of cell* division rates in the distal cambium* domain likely due to
229 high levels of PXY_{active}* (Figure 2B-E, Video 6, Video 7, Video 8). The cell* division
230 rate was highest in the central cambium* domain defined by high [PXY*] and by
231 moderate [PXY_{active}*] (Figure 2B-D, Video 8, Video 9, Video 10, Video 11). Also, not
232 only xylem* but also phloem* was continuously produced and the fate of cambium
233 cells* was dependent on their position relative to the differentiated tissues*. In the
234 central cambium* domain, cells* proliferated and constantly replenished the stem cell
235 pool (Figure 2B, Video 6, Video 7, Video 8). Thus, by incorporating relatively simple
236 rules, Model 2A comprised major cambium features, including phloem formation.
237 Moreover, in qualitative terms, the resulting anatomy* reproduced the anatomy of a
238 mature *Arabidopsis* hypocotyl (Figure 2A, E). It is interesting to note, however, while
239 the cambium domain stays almost perfectly circular in plants, the cambium* in our
240 simulations displayed a clear front instability suggesting that a stabilizing mechanism
241 exists which we missed in our model.

242

243 **Cambium model explains the effect of ectopic CLE41 expression**

244 To evaluate the predictive power of Model 2, we tested its capacity to simulate the
245 effects of genetic perturbation of cambium regulation. Ectopic expression of *CLE41*
246 by employing the *IRREGULAR XYLEM 3/CELLULOSE SYNTHASE CATALYTIC*
247 *SUBUNIT 7* (*IRX3/CESA7*) promoter, which is active in cells undergoing secondary

cell wall deposition [35-37], substantially alters hypocotyl anatomy [16]. This effect was confirmed when *PXYpro:CFP/SMXL5pro:YFP* activities were analyzed in a plant line carrying also an *IRX3pro:CLE41* transgene (Figure 3A, Figure 2—figure supplement 1, Figure 3—figure supplement 1, Figure 3—figure supplement 2, Figure 3—figure supplement 3, Figure 3—figure supplement 4). The *PXYpro:CFP* activity domain had a cylindrical shape including the proximal cambium domain and the xylem tissue itself in plants with a wild type background (Figure 2A, Figure 3—figure supplement 1, Figure 3—figure supplement 2, Figure 3—figure supplement 3, Figure 3—figure supplement 4). While in the presence of the *IRX3pro:CLE41* transgene, *PXYpro:CFP* activity was found in irregularly shaped patches containing differentiated xylem vessel elements distributed over the whole cross-section (Figure 3A, Figure 3—figure supplement 1, Figure 3—figure supplement 2, Figure 3—figure supplement 3, Figure 3—figure supplement 4). Moreover, we observed regions without *PXYpro:CFP* activity in proximal hypocotyl regions where *SMXL5pro:YFP* was active (Figure 3A, Figure 3—figure supplement 1, Figure 3—figure supplement 2, Figure 3—figure supplement 3, Figure 3—figure supplement 4). Besides, a substantial part of *SMXL5pro:YFP* activity was detected in the distal regions of the hypocotyl forming islands of irregular shape sometimes intermingled with *PXYpro:CFP* activity (Figure 3A, Figure 3—figure supplement 1, Figure 3—figure supplement 2, Figure 3—figure supplement 3, Figure 3—figure supplement 4). This activity pattern was in contrast to the one found in plants without the *IRX3pro:CLE41* transgene where *SMXL5pro:YFP* reporter activity surrounded the *PXYpro:CFP* expression domain only from the distal side (Figure 2A, Figure 3—figure supplement 1, Figure 3—figure supplement 2, Figure 3—figure supplement 3, Figure 3—figure supplement 4). These results indicated that not only the radial symmetry of the

hypocotyl [16] but also cambium organization depends on the site of CLE41 production.

To simulate the effect of the *IRX3pro:CLE41* transgene *in silico*, we instructed xylem cells* to produce CLE41* at the same rate as phloem cells* (Model 2B). Although in this case xylem* formation was initially repressed possibly due to high levels of PXY_{active}* in all cambium* cells (Figure 3B, Video 12, Video 13, Video 14), new xylem cells* were formed as soon as the distance between existing xylem and phloem cells* became large enough such that CLE41* levels and, in turn, [PXY_{active}*] dropped to permissive levels (Figure 3C, Video 12, Video 13, Video 14). New phloem cells* were produced close to existing phloem and xylem cells* likely due to high levels of PXY_{active}* (Figure 3C, Video 15, Video 16). As a result, Model 2B produced a similar disruption in cambium* organization, as observed in *IRX3pro:CLE41* plants (Figure 3D, Video 12, Video 13, Video 14). Zones with both high [PXY_{active}*] and low [PXY*], which were found in the distal cambium* in Model 2A (Figure 2E, Video 16, Video 17), appeared in the organ* center together with individual xylem cells* (Figure 3D). Moreover, in addition to being produced in distal regions, new phloem cells* were produced in the central areas of the organ* as demonstrated previously for *IRX3pro:CLE41* plants [16]. Thus, rules determining cambium* polarity implemented in Model 2 were sufficient to simulate organ anatomy found in wild type and *IRX3pro:CLE41* genetic backgrounds.

In contrast, a discrepancy between the model logic and the *in planta* situation was suggested when we compared a model having reduced PXY* activity with *pxy* mutants carrying the *PXYpro:CFP* and *SMXL5pro:YFP* reporters. In *pxy* mutants, the

298 xylem tissue did not have a cylindrical shape, but was instead clustered in radial
299 sectors showing *PXYpro:CFP* and, at their distal ends, *SMXL5pro:YFP* activity,
300 whereas regions in between those sectors had little to no xylem and did not show
301 reporter activity (Figure 3E, Figure 2—figure supplement 1, Figure 3—figure
302 supplement 1, Figure 3—figure supplement 2, Figure 3—figure supplement 3, Figure
303 3—figure supplement 4). Interestingly, *PXYpro:CFP* and *SMXL5pro:YFP* activity
304 domains were still mostly distinct meaning that *PXYpro:CFP* activity did not expand
305 further beyond established xylem than in wild type (Figure 3E, Figure 3—figure
306 supplement 5). This discrepancy indicated that, in contrast to our assumption, the
307 CLE41-PXY signaling module did not restrict *PXY* promoter activity in the distal
308 cambium. Of note, the sharp border between *PXYpro:CFP* and *SMXL5pro:YFP*
309 activity was less pronounced in *pxy* mutants mostly due to a spread of
310 *SMXL5pro:YFP* activity towards xylem tissues (Figure 3—figure supplement 5). The
311 discrepancy between Model 2 and the situation in plants was confirmed when we
312 completely eliminated PXY* activity from our model (Model 2C). As expected, this
313 elimination resulted in the absence of growth due to the full dependence of cell*
314 divisions on the PXY* function, clearly being at odds with the phenotype of *pxy*
315 mutants (Figure 3E). Even when we only reduced PXY* activity (Model 2D), this did
316 not result in a split of the continuous cambium domain* but abolished phloem*
317 formation and increased the production of xylem* (Figure 3F).

318

319 Interestingly, the quantification of water transporting xylem vessels, xylem fibers,
320 which provide mechanical stability, and xylem parenchyma in sections from wild type
321 and *pxy* mutant hypocotyls by automated image segmentation revealed that the total
322 number of xylem cells and the number of xylem vessels was comparable (Figure 3G-

323 I, Figure 3—figure supplement 6). In contrast, the number of cells classified as fibers
324 was substantially reduced in *pxy* mutants whereas the number of cells classified as
325 parenchyma was increased (Figure 3G-I). These results suggested that during radial
326 growth, *PXY* promotes the fiber-parenchyma ratio in the xylem, while the formation of
327 xylem vessels and the total number of cambium-derived cells produced toward the
328 xylem is hardly *PXY*-dependent.

329

330 **Multiple phloem-derived factors determine cambium activity**

331 Our observations prompted us to reconsider some features of the model and to
332 extend our 'French flag' approach. As the proximal cell production rate by the
333 cambium was not *PXY*-dependent, we made xylem* formation independent from the
334 control of PXY-active*. Instead, cambium cells* differentiated into xylem cells* when
335 they reached a specific size and, at the same time, expressed PXY* as a positional
336 feature. To maintain a population of active cambium cells* in the absence of PXY*,
337 we introduced a second phloem*-derived factor (PF), reminiscent of the PEAR
338 transcription factors identified recently [12]. PF* stimulated cell* divisions by
339 promoting the production of a division factor (DF) in cambium cells* and in phloem
340 parenchyma* (Figure 4A, Figure 4—figure supplement 1, see below). Cambium cells*
341 divided only if the concentration of DF* exceeded a threshold value (Supplementary
342 File 1). DF* production was at the same time stimulated by PXY_{active}* as its only effect
343 in cambium cells* (Figure 4A). Thereby, cambial cell* divisions were dependent on
344 the combined influence of PXY_{active}* and their proximity to phloem poles* (see below).

345 PF* was, thus, produced in phloem poles* and the levels in other cells* were
346 determined by the diffusion and degradation:

$$\frac{d}{dt}[PF^*] = production_{PF} + diffusion_{PF} - degradation_{PF} \cdot [PF^*] \quad (5)$$

DF* production was, in turn, determined as follows:

$$\frac{d}{dt}[DF^*] = diffusion_{DF} + \frac{production_{DF*}([PF*]+100*[PXY^*_{active}])}{(K+[PF^*]+100*[PXY^*_{active}])} - degradation_{DF} \quad (6)$$

Where K stands for an empirically defined parameter capping the production rate of DF*.

Based on the strong association of xylem sectors with developing phloem cells (Figure 3E), we further hypothesized that the formation of those sectors in *pxy* mutants was dependent on the heterogeneity of cell type distribution in the phloem. Therefore, phloem cells* from the previous models were split into two cell types – phloem parenchyma* and phloem poles* (Figure 4A, Figure 4—figure supplement 1). To achieve the dispersed pattern of phloem poles, cambium-derived cells* fulfilling the criteria to differentiate into phloem* (see above), differentiated into phloem poles* by default, unless inhibited by PF*, which was specifically produced in pole cells* (Supplementary File 1). Thereby, phloem poles* suppressed phloem pole* formation in their vicinity, expected to result in a patchy pattern of phloem poles as observed *in planta* [38]. The inhibition of phloem poles in their immediate environment is reminiscent to the CLE45/RECEPTOR LIKE PROTEIN KINASE 2 (RPK2) signaling cascade restricting protophloem sieve element identity to its usual position [39, 40]. It is worth noting that in our model, CLE41* was still produced in both phloem poles* and phloem parenchyma* but with a higher rate in phloem poles*. To further achieve PXY*-independent cambium subdomain separation, phloem parenchyma* and

phloem poles* were set to express another diffusive signal (RP) which suppressed PXY* expression in cambium* cells, the role that was played by PXY_{active}* before (Figure 4A, Figure 4—figure supplement 1, Supplementary File 1). The role of RP is reminiscent to the role of cytokinin which inhibits xylem-related features in tissue domains designated for phloem development [41]. Importantly, cell divisions in the distal cambium* were not actively repressed anymore but were exclusively dependent on cell size and the level of DF* (Supplementary File 1).

The implementation of these principles *in silico* (Model 3A) resulted again in the establishment of two cambium* subdomains – the distal subdomain which was characterized by high concentrations of DF* and the proximal subdomain characterized by high PXY* concentration (Figure 4B-D, Figure 4—figure supplement 1, Video 18, Video 19, Video 20, Video 21, Video 22, Video 23). Distally, the cambium* produced phloem parenchyma cells* from which phloem poles* were continuously formed with a pattern resembling the patchy phloem pattern observed in plants (Figure 4B, Figure 4—figure supplement 1) [38, 42]. Interestingly, the localization of PF* production mainly in phloem poles* resulted in increased DF levels in the vicinity of those poles and, consequently, in locally increased cell* division rates (Video 20, Video 21). This observation is in line with the observation that phloem poles drive cell divisions in their immediate environment and that phloem cells still divide after initial specification [12, 14]. When comparing the radial pattern of *PXYpro:CFP/SMXL5pro:YFP* activities and, as an *in silico* approximation to these activities, the distribution of PXY* and DF* in our model over time, patterns were stable in both cases (Figure 4B, Figure 3—figure supplement 1, Figure 3—figure supplement 2, Figure 3—figure supplement 3, Figure 3—figure supplement 4, Video

18, Video 22, Video 23). This demonstrated that our model was able to generate stable radial patterns of gene* activity comparable to the *in planta* situation.

By instructing CLE41* production additionally in xylem cells*, we next simulated CLE41-misexpression by the *IRX3* promoter (Model 3B, Figure 4—figure supplement 1, Figure 4E, Video 24, Video 25, Video 26, Video 27, Video 28, Video 29). CLE41* interacted with PXY* on the proximal cambium* border, which resulted in ectopic DF* production and phloem-parenchyma* formation in the proximal hypocotyl* regions (Figure 4E, Video 24, Video 28), similarly as during radial hypocotyl growth in *IRX3pro:CLE41* plants (Figure 3A, Figure 3—figure supplement 1, Figure 3—figure supplement 2, Figure 3—figure supplement 3, Figure 3—figure supplement 4). Still, xylem cells* were formed, generating a patchy xylem* pattern resembling the xylem configuration found in *IRX3pro:CLE41* plants (Figure 3A, Figure 4E, Video 24).

Fully eliminating CLE41* binding to PXY* and therefore PXY* activity but keeping the positional information of PXY* for xylem cell differentiation (Model 3C, Figure 4—figure supplement 1,) generated a patchy outline of the distal cambium* subdomain (Figure 4F, Video 30, Video 31, Video 32, Video 33, Video 34, Video 35). While PXY* was usually the main trigger of cell* divisions in cambium cells* at a certain distance from phloem poles*, PF* was sufficient for triggering cell divisions next to phloem poles*. Heterogeneous cambium activity was already observable at early phases of radial hypocotyl growth *in silico* and *in planta* and resulted overall in a reduced tissue production in both systems (Figure 4F, Figure 3—figure supplement 1, Figure 3—figure supplement 2, Figure 3—figure supplement 3, Figure 3—figure supplement 4, Video 30, Video 31, Video 32, Video 33, Video 34, Video 35). Thus, by introducing

both a PXY*-independent pathway stimulating cambium* proliferation and a dependence of cell* proliferation on the distance to phloem poles*, we were able to simulate important features of the *pxy* mutant phenotype (Figure 3E, Figure 4F, Figure 3—figure supplement 1, Figure 3—figure supplement 2, Figure 3—figure supplement 3, Figure 3—figure supplement 4). Collectively, we concluded that we established a computational cambium model sufficiently robust to simulate major genetic perturbations of cambium regulation.

Physical properties of cambium-derived cells have the potential to influence stem cell behavior

Next, we were interested to see whether the established model was able to reveal organ-wide features of radial plant growth. A characteristic of cambium stem cells is that they divide mostly in periclinal orientation, which is in parallel to the organ surface, resulting in the frequent formation of radial cell files (Figure 2A). Interestingly, although the overall tissue anatomy of the modelled organ* resembled the *in planta* situation, cell division orientation in our model outputs was almost random suggesting that radial cell file formation cannot be explained by the molecular signaling pathways implemented into the model (Figure 4A). The strong dominance of periclinal divisions *in planta*, however, implies the presence of a positional signal instructing cell division orientation. Because classical observations indicated that physical forces play a role in this regard [43-45], we tested whether the model was suited for finding indications for the influence of differential cell stiffness on geometric features of radial plant growth.

444 To do so, we first determined the relative cell wall thickness in hypocotyl cross
445 sections using the cell wall dyes Direct Yellow 96 and Direct Red 23 [46] as an
446 indication. Notably, staining intensities were approximately half as strong compared
447 to cells of the surrounding tissue (Figure 4—figure supplement 2). Expecting that
448 staining intensities correlate with cell wall stiffness and by also taking into account
449 results obtained previously by Atomic Force Microscopy of the cambium region [47],
450 we assumed that cambium stem cells are half as stiff as surrounding cells and
451 integrated this feature into our model by expanding VirtualLeaf to allow for the
452 integration of cell-type specific wall stiffness (see Supporting Information "VirtualLeaf
453 Simulations" for details). We implemented this information in the Hamiltonian
454 operator, which is used to approximate the energy of the system and takes both
455 turgor pressure and cell wall resistance into account. In practice this means that a
456 higher cell wall stiffness will increase the cell walls' resistance to being stretched and
457 will result in slower cell* growth.

458

459 Utilizing this expanded model (Model 4), we investigated the parameter space to find
460 parameters accurately describing cambium activity not only qualitatively but also
461 quantitatively. To incorporate realistic tissue ratios and unbiased parameter
462 identification, we performed an automated parameter search using a previous
463 characterization of Arabidopsis hypocotyl anatomy [38] as a criterion for parameter
464 selection. To this end, we evaluated our searched parameter sets to aim for a cell
465 type distribution of 24, 10 and 65 % for cambium*, xylem*, and phloem cell* number,
466 respectively. Performing 12,500 simulations resulted in n = 5 parameter sets
467 (Supplementary File 2), which produced more realistic cell type proportions than we
468 achieved by our manually selected set before (Figure 4G, Figure 4—figure

supplement 3). Thus, by taking real cell type proportions as a guideline for parameter search, we were able to establish a model generating a more realistic morphology as a solution. Furthermore, by generating several parameter sets that described the experimentally observed tissue ratios equally well, we demonstrated that even with differing parameter values the model behavior remained consistent reaffirming the model structure we had identified with Model 3A and was parameterized in Model 4 (Figure 5A, B, Figure 4—figure supplement 3, Video 36, Video 37, Video 38, Video 39, Video 40, Video 41).

To next investigate the role of biomechanics in the direction of cell division, we analyzed the model behavior at different cell wall stiffness values. Specifically, we were interested in the role of xylem* and epidermis*, the latter being represented by the relative perimeter stiffness of the outer tissue boundary in VirtualLeaf. Of note, defining the outer cell* layer as epidermis* was done for simplicity reasons as the rather complex periderm usually forms the outer tissues of older hypocotyls [48]. Here, we assumed xylem or epidermis cells* and, in turn, the relative perimeter stiffness to be more resistant to expansion due to the thickness of their cell walls* and implemented this behavior in Model 4 as a cellular* property. First we explored how the variation of the stiffness of xylem cell walls* impacted tissue formation (Figure 5C, Video 42, Video 43, Video 44, Video 45, Video 46, Video 47), we first observed that, as expected, increasing cell wall* stiffness led to a xylem*-specific decrease in cell* size and major axis length (Figure 5—figure supplement 1A, B). In turn, some cambium cells showed an increase in length as the cell type* with the closest proximity to xylem cells*. In addition, we observed a general decrease in the number of cells*, particularly of xylem cells* (Figure 5—figure supplement 1D). We

494 explained this effect by a ‘physical’ constraint generated by ‘stiffer’ xylem cells* acting
495 on neighboring cambium cells* impairing their expansion and, thus, their
496 transformation into xylem* (Video 42, Video 43, Video 44, Video 45, Video 46, Video
497 47). Importantly, neither cell area nor cell length was affected in phloem cells* and
498 the number of cambium cells* stayed constant (Figure 5—figure supplement 1),
499 suggesting that the general growth dynamics of the model and especially the
500 behavior of cambium cells* was comparable under the different stiffness* regimes.
501 When analyzing the same characteristics for the different epidermis* tissue regimes
502 (Figure 5D, Video 48, Video 49, Video 50, Video 51, Video 52), we found that neither
503 cell size* nor cell length* were impacted (Figure 5—figure supplement 2). Instead, we
504 found a decrease in the number of cells* per simulation with increasing cell wall
505 stiffness, in particular phloem parenchyma* and phloem pole cells*, as the increased
506 resistance of the outer tissue boundary limited the overall tissue growth resulting in
507 less cells being produced in the outer parts of the tissue (Figure 5—figure
508 supplement 2).

509

510 To access the effect of increased stiffness of xylem and epidermis cell walls* on cell*
511 division orientation, we first defined cell lineages* as groups of cells* having
512 originated from the same precursor cell* and drew lines between immediate daughter
513 cells* (Figure 5E, F). We then calculated the goodness of fit (R^2) of a linear
514 relationship between center of mass coordinates of all individual lines as a proxy for
515 lineage* ‘radiality’ and, thus, for the ratio of periclinal versus anticlinal cell divisions*.
516 After obtaining the R^2 value for each lineage*, we tested for median differences
517 among r distributions under each stiffness regime (Figure 5G, Figure 5—figure
518 supplement 3). These comparisons showed that the increase of the xylem* to non-

519 xylem cell wall* stiffness ratio produced a shift from more “curved” lineages (R^2 <
520 0.25) towards more radial lineages* (R^2 > 0.75) (Figure 5G, Figure 5—figure
521 supplement 3A). We attributed this effect to an increased radial elongation of
522 cambium cells* with increasing xylem stiffness* (Video 42, Video 43, Video 44, Video
523 45, Video 46, Video 47) and the preferred cell division* along the shortest axis in
524 VirtualLeaf [32]. Although the effect of xylem cell* stiffness on lineage radiality was
525 not on all lineages, as a fraction of them remained less radially oriented even for high
526 xylem stiffness (Figure 5G), implementing stiffness as a cell property therefore
527 produced coherent results in terms of the appearance of radial cell files* as an
528 emergent property of xylem cell* wall stiffness. In contrast, the analysis of different
529 epidermis cell wall stiffness did not show a clear change in the distribution of lineages
530 in the range of analyzed stiffness regimes (Figure 5H, Figure 5—figure supplement
531 3B, Video 48, Video 49, Video 50, Video 51, Video 52) as increasing stiffness limited
532 tissue growth and therefore the formation of cell lineages. These results remained
533 consistent for both xylem* and epidermis* stiffness regimes when varying other
534 parameters determining cell wall dynamics, i.e. the target length of cell wall elements
535 and the yielding threshold for the introduction of new cell wall segments (Figure 5—
536 figure supplement 4).

Discussion

Growth and development of multicellular organisms are complex non-linear processes whose dynamics and network properties are not possible to predict only based on information on their individual building blocks and their one-to-one interactions. The rather simple cellular outline along the radial axes of plant organs, growth in only two dimensions, and the recent identification of central functional properties [11-13], make radial plant growth an attractive target for a systematic approach to reveal its intriguing dynamics. Here, we developed a computational model representing a minimal framework required for radial plant growth using the VirtualLeaf framework [32]. In particular, we combined an agent-based model of the tissue layout with an ODE model of the inter-cellular PXY/CLE41 signaling module. By integrating these two modeling and biological scales, we were able to recapitulate not only the complex behaviors that arise as consequence of the cellular interactions [49] but also the interplay between cellular layout and intercellular signaling dynamics. Therefore, our model allows analyzing fundamental features of plant organ growth and integrates the PXY/CLE41 module as one central element for cambium patterning and maintenance.

Using positional information mediated by morphogenetic gradients of diffusible chemicals to pattern growing structures is a classical concept in developmental biology which has stirred a long history of fundamental debates [50]. Initially, we used the PXY/CLE41 module to generate such a gradient instructing cambium cells* to differentiate into xylem cells*, to proliferate or to differentiate into phloem cells*. Repression of cell division in the distal cambium was achieved by implementing an inhibitory feedback loop of PXY-signaling* on PXY* production. Altogether, this setup

562 was already sufficient to maintain stable radial tissue organization during radial
563 growth and established a maximum of cell division rates in the cambium center as
564 observed by experimental means [13]. Thus, we conclude that cambium organization
565 and radial patterning of plant growth axes can be maintained by a distinct pattern of
566 radially acting morphogens. Such a role was initially proposed for auxin whose
567 differential distribution, however, seems to be rather a result of tissue patterning than
568 being instructive for radial tissue organization [51].

569

570 In contrast to expected roles of the *PXY* pathway in xylem formation based on
571 experiments during primary vascular development [19, 22, 24], we observed that the
572 overall amount of proximal tissue production during radial plant growth did not
573 depend on the *PXY* function. Automated image analysis including object
574 classification revealed that neither the number of cells produced toward the organ
575 center nor the number of vessel elements did change in a *pxy* mutant background
576 but rather the ratio between parenchyma and fiber cells. Therefore, in contrast to a
577 negative effect of PXY/CLE41 signaling on vessel formation in vascular bundles in
578 leaves [19, 24], vessel formation during radial plant growth is *PXY/CLE41*-
579 independent. Instead, fiber formation is positively associated with the *PXY/CLE41*
580 module. These observations indicated that xylem formation is unlikely to be
581 instructed by PXY/CLE41 signaling alone and that additional signals are required.

582

583 Moreover, the application of markers visualizing cambium organization showed that
584 *PXY*-deficiency leads to cambium disorganization in some regions of the hypocotyl
585 whereas in other areas, cambium anatomy is maintained. Since such areas are
586 regularly spaced, this pattern may arise due to factors acting in parallel to

PXY/CLE41 and which also carry spatial information. Although ethylene signaling was reported to act in parallel to PXY/CLE41 signaling, spatial specificity does not seem to be a characteristic property of ethylene signaling [52]. In contrast, PEAR transcription factors are phloem-derived and stimulate the proliferation of cambium stem cells presumably in a PXY/CLE41-independent manner [12] and, thus, may act similarly to the PF* factor we introduced in our model. The ERECTA/EPIDERMAL PATTERNING FACTOR-LIKE (ER/EPFL) receptor-ligand pathway acting in concert with the PXY/CLE41 module [53, 54] represents another candidate for playing such a role. In addition, CLE45 was recently proposed to be expressed in developing sieve elements, the conducting units of the phloem, and repress the establishment of sieve element identity in their immediate environment mediated by the RPK2 receptor protein [39]. The PF* factor in our model combines features of these phloem-derived molecules.

In addition to the phloem sending out instructive signals, early xylem cells have been identified to act as an organizing center of cambium patterning [11]. Although this finding seems to be at odds with our claim that phloem-derived signals are sufficient for cambium organization, it is important to consider that we ignored, for example, upstream regulation of postulated factors like PXY* or CLE41*, which obviously depends on positional information which could be mediated in plants by auxin or cytokinin signaling [55]. For simplicity, we also ignored organizing effects of signaling longitudinally to cross sections as it can, for example expected for polar auxin transport [56-58] in the context of cambium activity or xylem formation. Although being considerably more complex, the establishment of 3D models will be crucial essential for addressing this aspect.

612

613 In this context, it is interesting to note that we deliberately excluded the transition
614 from the initially bisymmetric tissue conformation to a concentric tissue organization
615 as it occurs in hypocotyls and roots [11, 38] from our model. Our rationale was that
616 the rather complex change in tissue anatomy from a primary to a secondary
617 conformation in the hypocotyl required more assumptions in our model and would
618 have spoiled the advantages of a relatively simple anatomy for generating a cell-
619 based computational model. Moreover, the differences in primary anatomy of shoots
620 and roots before the onset of radial plant growth [11, 59] would have required
621 different cellular outlines for both cases and, thus, would have hampered the
622 generality of our approach.

623

624 Interestingly, the front of cambium domains is very stable, i.e. almost perfectly
625 circular, *in planta* but this is not the case for our computational simulations. We
626 believe that instability in the computational models is due to local noise in the cellular
627 pattern leading to differential diffusion of chemicals* with respect to their radial
628 position and to a progressive deviation of domains from a perfect circle. Such a
629 deviation seems to be corrected by an unknown mechanism *in planta* but such a
630 corrective mechanism is, due to the absence of a good indication *in planta*, not
631 implemented in our models. Analyses of wt and *pxy* lines at different stages (Figure
632 3—figure supplement 1 and Figure 3—figure supplement 2, Figure 3—figure
633 supplement 3, Figure 3—figure supplement 4) revealed ‘gaps’ in the cambium
634 domain already at early stages of *pxy* development arguing against the possibility
635 that the *pxy* anatomy is caused by increased front instability. Although a corrective
636 mechanism ensuring front stability *in planta* is difficult to predict, our model now

637 allows to test respective ideas like directional movement of chemicals or stabilizing
638 communication between cells during cambium activity. In this context it is interesting
639 that increasing epidermis* 'stiffness' increased circularity of the growing organ* which
640 may be administered by the periderm [48], the protective cell layers which we did not
641 consider in our model.

642

643 Current research on plant mechanical biology indicates how cell mechanical
644 properties influence cell and tissue morphogenesis. Microtubules, turgor pressure
645 and cell wall composition are central factors in this regard [60, 61]. Due to the
646 geometric constraints in a radially growing plant axis, it becomes challenging to
647 uncouple these factors experimentally and to establish the impact of one factor on
648 organ patterning during radial plant growth. By expanding VirtualLeaf to allow for the
649 integration of cell type-specific wall stiffness, we fundamentally increased the
650 spectrum of potential modeling approaches. In particular, since cell wall stiffness is
651 accessible by the cellular model throughout simulations, it is now possible to simulate
652 and analyze e.g. the dynamics of auxin or brassinosteroid-mediated cell wall
653 loosening [62, 63]. In our cambium model, by modulating exclusively cellular
654 'stiffness', we were able to computationally simplify the 'physical' properties and,
655 thereby, develop a hypothesis how inter-tissue forces influence stem cell behavior
656 not only cell autonomously, but also in a non-cell autonomous manner.

657

658 Taken together, we envision that the model presented in this study recapitulates the
659 qualitative and quantitative variation in radial plant growth on multiple levels, found in
660 different mutants or when comparing different dicotyledonous species [64].
661 Remarkable features like the establishment of concentric cambium rings often found

662 in the order of *Caryophyllales* [65] or ‘phloem wedges’ found in the *Bignonieae* genus
663 [66] may be recapitulated by adjusting the model’s parameters values or by
664 introducing additional factors. In the future, the model may help to predict targets of
665 environmental stimuli inducing changes of cambium activity like seasonal changes
666 [67] or mechanical perturbation [68], allowing the generation of testable hypotheses.
667 Thus, our dynamic model will be a useful tool for investigating a process not possible
668 to observe in real time and partly develops over exceptionally long periods.

669

670 # Material and Methods

671

672 ## Plant material and growth conditions

673 *Arabidopsis thaliana* (L.) Heynh. plants of Columbia-0 accession were used for all
674 experiments and grown as described previously [23]. *pxy-4* (SALK_009542,
675 N800038) mutants were ordered from the Nottingham Arabidopsis Stock Centre
676 (NASC). Plant lines carrying *IRX3pro:CLE41* and *35Spro:CLE41* transgenes [16]
677 were kindly provided by Peter Etchells (Durham University, UK). *PXYpro:ECFP-ER*
678 (*pPS19*) and *SMXL5pro:EYFP-ER* (*pJA24*) reporter lines expressing fluorescent
679 proteins targeted to the endoplasmatic reticulum (ER) were described previously [69,
680 70]. After sterilization, seeds were stratified for 2-3 days in darkness at 4ºC. Plants
681 were then grown at 21°C and 60 % humidity. To check *PXYpro:CFP/SMXL5pro:YFP*
682 activities, 27or 39-day-old seedlings were used. 27-day-old seedlings were grown on
683 plates in short-day conditions (10 h light and 14 h darkness). 39-day-old seedlings
684 were grown on soil in short-day conditions for 21 days and then moved to long-day
685 conditions (16 h light and 8 h darkness) for 18 days.

686

687 ## Confocal microscopy

688 Hypocotyls were isolated and cleaned from surrounding leaf material using razor
689 blades (Classic Wilkinson, Germany). The cleaned hypocotyls were mounted in 7 %
690 low melting point agar (Sigma-Aldrich, St. Louis, MO, USA) in water and sections
691 were generated using a vibratome (Leica VT1000 S). For monitoring hypocotyl
692 development, the developmental gradient in hypocotyls of 27 day-old plate-grown
693 plants (stages 1-3 shown in Figure 3—figure supplement 1A-C, E-G, I-K and Figure

3—figure supplement 2 A-C, E-G, I-K) was employed: the lower region close to the hypocotyl-root boundary was taken as the youngest stage (stage1), the middle region as stage 2, and the upper region close to the cotyledons as stage 3. As stage 4, sections from the middle region of 39 day-old plants grown on soil were taken which are shown in all other images displaying confocal analyses. For Figure 4—figure supplement 2A, B, 75 µm thick sections from soil-grown 32 day-old plants were stained for 60 minutes with 0.1 % w/v Direct Yellow 96 (Sigma Aldrich, St. Louis, US, S472409-1G) diluted in ClearSee [46] (10 % w/v xylitol, 15 % w/v sodium deoxycholate, 25 % w/v urea), washed three times with ClearSee and mounted in ClearSee on microscope slides. For other experiments, 60 µm thick sections were stained for 5 minutes with 0.1 % w/v Direct Red 23 (Sigma Aldrich, St. Louis, US, 212490-50G) diluted in water, washed three times with water and mounted in water on microscope slides. For analyzing the fluorescent markers, a Leica SP8 or Stellaris 8 (Leica, Germany) confocal microscope was used. Different fluorescence protein signals were collected in different tracks. YFP was excited at 514 nm and emission was collected at 522-542 nm. CFP was excited at 458 nm and the signal emission was collected at 469-490 nm. The Direct Red 23-derived signal was excited at 495 nm and emission was detected at 558-649 nm. The Direct Yellow 96-derived signal was excited at 488 nm and emission was detected at 500-540 nm. For qualitative comparisons, 5-10 samples for each sample type were included and repeated at least twice. Please, be aware that, depending on variations in staining intensity, sometimes cell walls of vessel elements appear white in the provided images due to the overlap of signal from Direct Red 23 staining and autofluorescence captured during *PXYpro:CFP* detection (see for example Figure 3—figure supplement 2D).

Ilastik cell type counting

720 For cell type classification and quantification, sections were produced from 42 day-
721 old plants as previously described [23]. The xylem area was cropped manually from
722 histological images of wild type and *pxy* mutant. The Ilastik toolkit [71] was used for
723 image segmentation and cell type classification (https://www.ilastik.org). With a
724 training set, the pixel classification workflow was trained to distinguish cell walls from
725 the background. After segmentation, the object classifier was then trained to split the
726 resulting objects into four groups - xylem vessels, xylem fibers, xylem parenchyma,
727 and unclassified objects. The resulting classifier was then applied to all cropped
728 images. For each image, cell type data were extracted using python. 11-12 plants
729 each for wild type and *pxy* mutants were compared in two independent experiments.
730

731 **VirtualLeaf simulations**

732 Simulations were performed as recommended previously [32]. To be able to see
733 established models in action, the VirtualLeaf software was installed according to the
734 following instructions described in the Appendix 1 and as described previously [72].
735 All simulations within Model 1, Model 2, Model 3, and Model 4 respectively, were
736 conducted for the same VirtualLeaf time duration and repeated at least ten times to
737 account for the stochastic nature of the tissue simulations (for details on simulations
738 in VirtualLeaf, see section “Description of the VirtualLeaf simulations” in the Appendix
739 1). Dilution of the modelled variables due to growth has been omitted.
740

741 **Splitting the result of VirtualLeaf simulations into bins**

742 After a VirtualLeaf simulation was completed, the resulting xml template was stored.
743 To analyze the distribution of chemicals* in such a template along the radial axis, we
744 produced a python script named “Cambium_bins_calculation.ipnb”. Within the script,
745 it was possible to indicate the path to the xml file, and the script produced two .csv

files – one with a table containing data about each cell and another with information about averages across the requested bin number. Cells were sorted into bins based on the cells' Euclidean distance from the center of the tissue, which was defined as the average of the x- and y-coordinates of all the cells in the tissue.

Parameter estimation and exploration of the parameter space

To estimate the model parameters and, at the same time, investigate the parameter space, we performed a large set of simulations with randomized parameters to identify feasible parameter combinations. In particular, we employed a combination of python and shell scripting to set up the parameter sets, run the simulations and analyze the results. To generate the parameter sets we followed the tutorial using the python library xml.etree.Elementree as described [33]. The search intervals were defined based on the manually determined parameter values of model 3A: The search interval was set between 1/3 and 3-times the original value. The individual parameter sets were then simulated for a duration of t_simulated = 2200 steps on a computing cluster (Linux, 64-bit). The resulting xml leaf was then analyzed based on tissue size and proportions. Based on *in planta* observations [38], we determined that the simulation should result in 24 % cambium, 10 % xylem, and 65 % phloem cells. As all tissues are equally important, we used a weighted least squares scoring function to compare the experimentally measured tissue ratios with the model simulations. We added a term for the total number of cells to favor parameter sets that resulted in tissue growth. Altogether, this resulted in the following scoring function:

$$x_{sim} = \frac{1}{0.01}\left(0.1 - fraction_{xylem}\right)^2 + \frac{1}{0.05676}(0.24 - fraction_{cambium})^2 + \frac{1}{0.4225}\left(0.65 - fraction_{phloem}\right)^2 + (1 - total\ cells/3000)^2$$

As we were interested in obtaining simulations with an active cambium we discarded simulations that resulted in hypocotyls* with less than 300 cells* in total and with cambium cells less than 30. We further eliminated any parameter sets with pronounced edge instability.

Exploration of stiffness

To explore the effects of stiffer (i.e. less flexible) xylem cell walls and epidermis cell walls as represented by the perimeter stiffness, we slightly modified the VirtualLeaf code so that it was possible for λ_L (the "cost" of deviation of the wall element's length from the target length) to assume cell type-specific values. More specifically, we defined a new parameter named $cell\ wall\ stiffness$, and set $\lambda_L = cell\ wall\ stiffness$ according to the experimentally determined cell wall thickness as a proxy for cell wall stiffness. We then ran the model with different ratios of $cell\ wall\ stiffness$ compared to the normal parameter value, while maintaining the same tissue configuration used for the other simulations done within this study. The values chosen for the parameter were 0.1, 0.5, 1, 5, 10-fold change for both tissues of interest and 50-fold change for xylem*. We replicated each run 30 times. We further repeated the analysis of different stiffness regimes while varying other cell wall dynamic parameters by +/- 50%, i.e. the target element for cell wall elements and the yielding threshold for the introduction of new cell wall elements (for n=10 simulations per parameter combination).

To study the proliferation trajectory of cells, we performed for every lineage a linear regression of the centers of mass for the cells belonging to that lineage, and used the coefficient of determination (R^2) as proxy for proliferation trajectory of the lineage. We

795 next tested for median differences among the R^2 distribution under each stiffness
796 regime using the Kruskal-Wallis (KS) test, and performed the Dunn test to determine
797 differences among groups in case of significant KS. Before performing the KS, we
798 subsampled the data to maintain the same number of samples across stiffness
799 values, and bootstrapped the samples to obtain robust median estimators and
800 confidence intervals.
801
802 Statistical analyses and visualizations of 'stiffness' were performed using the R
803 language for statistical computing and graphics (https://www.r-project.org/), using the
804 tidyverse family of packages [73], together with the broom (https://cran.r-
805 project.org/web/packages/broom/index.html), FSA (https://github.com/droglenc/FSA),
806 and boot packages [74, 75].
807
808 **Material availability statement**
809 For each of the models and frameworks described in this paper, we provide code
810 files at https://github.com/thomasgreb/Lebovka-et-al_cambium-models.
811

Acknowledgements

We thank Peter Etchells (Durham University, UK) for providing seed material, Karin Grünwald and Martina Laaber-Schwarz (both GMI, Vienna, Austria) for technical assistance and Dongbo Shi, Eva-Sophie Wallner and Vadir López-Salmerón for comments on the experimental strategy and the manuscript. We also thank Claudiu Antonovici (University of Leiden, The Netherlands) for help in setting up the VirtualLeaf platform. This work was supported by the Deutsche Forschungsgemeinschaft (DFG) through the Research Unit FOR2581 'Plant Morphodynamics (grant GR2104/6), grant GR2104/4-1 and a Heisenberg Professorship (GR2104/5-2) to T.G.. The work by B.H.M. was initiated at Centrum Wiskunde & Informatica (CWI), Amsterdam, The Netherlands. R.M. and B.H.M. thank CWI for providing a CWI Internship to B.H.M. and for hosting I.L.. R.G. was supported by the CRC 1101 „Molecular Encoding of Specificity in Plant Processes" (DFG) and the Joachim Herz Stiftung.

Conflict of Interest

The authors have no conflicts of interest to declare.

Supplementary Information Items

Figure 3—figure supplement 1: First example revealing the dynamics of *PXYpro:CFP/SMXL5pro:YFP* activities during radial hypocotyl growth in wild type, *IRX3pro:CLE41* and *pxy* plants.

Figure 3—figure supplement 2: Second example revealing the dynamics of *PXYpro:CFP/SMXL5pro:YFP* activities during radial hypocotyl growth in wild type, *IRX3pro:CLE41* and *pxy* plants.

Figure 3—figure supplement 3: First example revealing the dynamics of *PXYpro:CFP/SMXL5pro:YFP* activities during radial hypocotyl growth in wild type, *IRX3pro:CLE41* and *pxy* plants (color-blind mode).

Figure 3—figure supplement 4: Second example revealing the dynamics of *PXYpro:CFP/SMXL5pro:YFP* activities during radial hypocotyl growth in wild type, *IRX3pro:CLE41* and *pxy* plants (color-blind mode).

Figure 3—figure supplement 5: Close-up revealing the dynamics of *PXYpro:CFP/SMXL5pro:YFP* activities in hypocotyls in wild type and *pxy* plants.

Figure 3—figure supplement 6: Overview and magnification of sections used for cell type classification shown in Fig. 3G-I.**Figure 3—Source data 1:** Source data for cell type classification using ilastik.

Figure 4—figure supplement 1: Overview of cell types*, regulatory interactions and expression* profiles in Model 3.

852 **Figure 4—figure supplement 2:** Determination of cell wall thickness across the
853 radial sequence of hypocotyl tissues.

854 **Figure 4—figure supplement 3:** Behavior of the different model parameterizations
855 (Model 4:2-5)

856 **Figure 5—figure supplement 1:** Distribution of cell* properties under different xylem
857 'stiffness' regimes.

858 **Figure 5—figure supplement 2:** Distribution of cell* properties under different tissue
859 boundary (=epidermis*) 'stiffness' regimes.

860 **Figure 5—figure supplement 3:** Fraction of median relative amount of cell lineages
861 for parameter sets 2-5.

862 **Figure 5—figure supplement 4:** Fraction of median relative amount of cell lineages
863 at different parameters governing cell wall* dynamics.

864

865 **Supplementary File 1:** Table listing cell* behavior rules for Models 1-4.

866 **Supplementary File 2:** Table listing parameter values and chemical thresholds
867 after parameter estimation.

868

869 **Appendix 1:** Instructions for implementing VirtualLeaf models.

870

871 **Video 1:** Model 1 output, visualizing xylem (red) and phloem (purple), and
872 accumulation of PXY* (blue) and PXY_{active}* (green)

873 **Video 2:** Model 1 output, visualizing CLE41* (yellow) accumulation

874 **Video 3:** Model 1 output, visualizing cell divisions (red)

875 **Video 4:** Model 1 output, visualizing PXY_{active}*

876 **Video 5:** Model 1 output, visualizing PXY*

877 **Video 6:** Model 2A output, visualizing xylem (red) and phloem (purple), and
878 accumulation of PXY* (blue) and PXY-active* (green)

879 **Video 7:** Model 2A output, visualizing CLE41* (yellow) accumulation

880 **Video 8:** Model 2A output, visualizing cell divisions (red)

881 **Video 9:** Model 2A output, visualizing cell divisions (red) together with PXY*
882 (blue) and PXY-active* (green) accumulation

883 **Video 10:** Model 2A output, visualizing PXY_{active}*

884 **Video 11:** Model 2A output, visualizing PXY*

885 **Video 12:** Model 2B output, visualizing xylem (red) and phloem (purple), and
886 accumulation of PXY* (blue), and PXY-active* (green)

887 **Video 13:** Model 2B output, visualizing CLE41* (yellow) accumulation

888 **Video 14:** Model 2B output, visualizing cell divisions (red)

889 **Video 15:** Model 2B output, visualizing accumulation of PXY* (blue) and PXY-
890 active* (green)

891 **Video 16:** Model 2B output, visualizing PXY_{active}*

892 **Video 17:** Model 2B output, visualizing PXY*

Video 18: Model 3A output, visualizing xylem (red), phloem parenchyma (light purple), and phloem poles (dark purple), and accumulation of PXY* (blue) and the division chemical (DF)* (green)

Video 19: Model 3A output, visualizing CLE41* (yellow) accumulation

Video 20: Model 3A output, visualizing cell divisions (red)

Video 21: Model 3A output, visualizing accumulation of PXY* (blue) and PXY_{active}* (green)

Video 22: Model 3A output, visualizing PXY_{active}*

Video 23: Model 3A output, visualizing PXY*

Video 24: Model 3B output, visualizing xylem (red), phloem parenchyma (light purple), and phloem poles (dark purple), and accumulation of PXY* (blue) and the division chemical (DF)* (green)

Video 25: Model 3B output, visualizing CLE41* (yellow) accumulation

Video 26: Model 3B output, visualizing cell divisions (red)

Video 27: Model 3B output, visualizing accumulation of PXY* (blue) and PXY_{active}* (green)

Video 28: Model 3B output, visualizing PXY_{active}*

Video 29: Model 3B output, visualizing PXY*

Video 30: Model 3C output, visualizing xylem (red), phloem parenchyma (light purple), and phloem poles (dark purple), and accumulation of PXY* (blue) and the division chemical (DF)* (green)

Video 31: Model 3C output, visualizing CLE41* (yellow) accumulation

915 **Video 32:** Model 3C output, visualizing cell divisions (red)

916 **Video 33:** Model 3C output, visualizing accumulation of PXY* (blue) and the
917 division chemical (DF)* (green)

918 **Video 34:** Model 3C output, visualizing PXY_{active}*

919 **Video 35:** Model 3C output, visualizing PXY*

920 **Video 36:** Model 4 output, parameter Set 1, visualizing xylem (red), phloem
921 parenchyma (light purple), and phloem poles (dark purple), and
922 accumulation of PXY* (blue) and the division chemical (DF)* (green)

923 **Video 37:** Model 4 output, parameter set 1, visualizing CLE41* (yellow)
924 accumulation

925 **Video 38:** Model 4 output, parameter set 1, cell divisions (red)

926 **Video 39:** Model 4 output, parameter set 1, visualizing accumulation of PXY*
927 (blue) and the division chemical (DF)* (green)

928 **Video 40:** Model 4 output, parameter set 1, visualizing PXY_{active}*

929 **Video 41:** Model 4 output, parameter set 1, visualizing PXY*

930 **Video 42:** Model 4 output, visualizing accumulation of PXY* (blue) and the division
931 chemical (DF)* (green) implementing a 0.1-fold change in xylem* cell
932 wall stiffness

933 **Video 43:** Model 4 output, visualizing accumulation of PXY* (blue) and the division
934 chemical (DF)* (green) implementing a 0.5-fold change in xylem* cell
935 wall stiffness

936 **Video 44:** Model 4 output, visualizing accumulation of PXY* (blue) and the division
937 chemical (DF)* (green) at experimentally determined xylem cell wall
938 stiffness

939 **Video 45:** Model 4 output, visualizing accumulation of PXY* (blue) and the division
940 chemical (DF)* (green), implementing a 5-fold increase in xylem* cell
941 wall stiffness

942 **Video 46:** Model 4 output, visualizing accumulation of PXY* (blue) and the division
943 chemical (DF)* (green), a 10-fold increase in xylem* cell wall stiffness

944 **Video 47:** Model 4 output, visualizing accumulation of PXY* (blue) and the division
945 chemical (DF)* (green), a 50-fold increase in xylem* cell wall stiffness

946 **Video 48:** Model 4 output, visualizing accumulation of PXY* (blue) and the division
947 chemical (DF)* (green) implementing a 0.1-fold change in epidermis*
948 cell wall stiffness

949 **Video 49:** Model 4 output, visualizing accumulation of PXY* (blue) and the division
950 chemical (DF)* (green) implementing a 0.5-fold change in epidermis*
951 cell wall stiffness

952 **Video 50:** Model 4 output, visualizing accumulation of PXY* (blue) and the division
953 chemical (DF)* (green) at experimentally determined epidermis* cell
954 wall stiffness

955 **Video 51:** Model 4 output, visualizing accumulation of PXY* (blue) and the division
956 chemical (DF)* (green), implementing a 5-fold increase in epidermis*
957 cell wall stiffness

Video 52: Model 4 output, visualizing accumulation of PXY* (blue) and the division chemical (DF)* (green), a 10-fold increase in epidermis* cell wall stiffness

Literature

1. Greb, T., and Lohmann, J.U. (2016). Plant Stem Cells. Current biology : CB *26*, R816-821.
2. Fischer, U., Kucukoglu, M., Helariutta, Y., and Bhalerao, R.P. (2019). The Dynamics of Cambial Stem Cell Activity. Annual review of plant biology *70*, 293-319.
3. Chiang, M.H., and Greb, T. (2019). How to organize bidirectional tissue production? Curr Opin Plant Biol *51*, 15-21.
4. Haas, A.S., Shi, D., and Greb, T. (2022). Cell fate decisions within the vascular cambium–initiating wood and bast formation. Frontiers in Plant Science *13*.
5. Shi, D., Tavhelidse, T., Thumberger, T., Wittbrodt, J., and Greb, T. (2017). Bifacial stem cell niches in fish and plants. Current opinion in genetics & development *45*, 28-33.
6. Sabatini, S., Heidstra, R., Wildwater, M., and Scheres, B. (2003). SCARECROW is involved in positioning the stem cell niche in the Arabidopsis root meristem. Genes Dev *17*, 354-358.
7. Sarkar, A.K., Luijten, M., Miyashima, S., Lenhard, M., Hashimoto, T., Nakajima, K., Scheres, B., Heidstra, R., and Laux, T. (2007). Conserved factors regulate signalling in Arabidopsis thaliana shoot and root stem cell organizers. Nature *446*, 811-814.
8. Mayer, K.F., Schoof, H., Haecker, A., Lenhard, M., Jurgens, G., and Laux, T. (1998). Role of WUSCHEL in regulating stem cell fate in the Arabidopsis shoot meristem. Cell *95*, 805-815.
9. Daum, G., Medzihradszky, A., Suzaki, T., and Lohmann, J.U. (2014). A mechanistic framework for noncell autonomous stem cell induction in Arabidopsis. Proceedings of the National Academy of Sciences of the United States of America *111*, 14619-14624.
10. Pi, L., Aichinger, E., van der Graaff, E., Llavata-Peris, C.I., Weijers, D., Hennig, L., Groot, E., and Laux, T. (2015). Organizer-Derived WOX5 Signal Maintains Root Columella Stem Cells through Chromatin-Mediated Repression of CDF4 Expression. Developmental cell *33*, 576-588.
11. Smetana, O., Makila, R., Lyu, M., Amiryousefi, A., Sanchez Rodriguez, F., Wu, M.F., Sole-Gil, A., Leal Gavarron, M., Siligato, R., Miyashima, S., et al. (2019). High levels of auxin signalling define the stem-cell organizer of the vascular cambium. Nature *565*, 485-489.
12. Miyashima, S., Roszak, P., Sevilem, I., Toyokura, K., Blob, B., Heo, J.O., Mellor, N., Help-Rinta-Rahko, H., Otero, S., Smet, W., et al. (2019). Mobile PEAR transcription factors integrate positional cues to prime cambial growth. Nature *565*, 490-494.

13. Shi, D., Lebovka, I., Lopez-Salmeron, V., Sanchez, P., and Greb, T. (2019). Bifacial cambium stem cells generate xylem and phloem during radial plant growth. Development (Cambridge, England) *146*, dev171355.
14. Bossinger, G., and Spokevicius, A.V. (2018). Sector analysis reveals patterns of cambium differentiation in poplar stems. Journal of experimental botany *69*, 4339-4348.
15. Kucukoglu, M., Nilsson, J., Zheng, B., Chaabouni, S., and Nilsson, O. (2017). WUSCHEL-RELATED HOMEOBOX4 (WOX4)-like genes regulate cambial cell division activity and secondary growth in Populus trees. New Phytol *215*, 642-657.
16. Etchells, J.P., and Turner, S.R. (2010). The PXY-CLE41 receptor ligand pair defines a multifunctional pathway that controls the rate and orientation of vascular cell division. Development (Cambridge, England) *137*, 767-774.
17. Etchells, J.P., Mishra, L.S., Kumar, M., Campbell, L., and Turner, S.R. (2015). Wood Formation in Trees Is Increased by Manipulating PXY-Regulated Cell Division. Current biology : CB *25*, 1050-1055.
18. Fisher, K., and Turner, S. (2007). PXY, a Receptor-like Kinase Essential for Maintaining Polarity during Plant Vascular-Tissue Development. Current biology : CB *17*, 1061-1066.
19. Hirakawa, Y., Shinohara, H., Kondo, Y., Inoue, A., Nakanomyo, I., Ogawa, M., Sawa, S., Ohashi-Ito, K., Matsubayashi, Y., and Fukuda, H. (2008). Non-cell-autonomous control of vascular stem cell fate by a CLE peptide/receptor system. Proceedings of the National Academy of Sciences of the United States of America *105*, 15208-15213.
20. Morita, J., Kato, K., Nakane, T., Kondo, Y., Fukuda, H., Nishimasu, H., Ishitani, R., and Nureki, O. (2016). Crystal structure of the plant receptor-like kinase TDR in complex with the TDIF peptide. Nature communications *7*, 12383.
21. Zhang, H., Lin, X., Han, Z., Qu, L.J., and Chai, J. (2016). Crystal structure of PXY-TDIF complex reveals a conserved recognition mechanism among CLE peptide-receptor pairs. Cell research *26*, 543-555.
22. Hirakawa, Y., Kondo, Y., and Fukuda, H. (2010). TDIF peptide signaling regulates vascular stem cell proliferation via the WOX4 homeobox gene in Arabidopsis. Plant Cell *22*, 2618-2629.
23. Suer, S., Agustí, J., Sanchez, P., Schwarz, M., and Greb, T. (2011). WOX4 Imparts Auxin Responsiveness to Cambium Cells in Arabidopsis. Plant Cell *23*, 3247-3259.

1021 24. Kondo, Y., Ito, T., Nakagami, H., Hirakawa, Y., Saito, M., Tamaki, T., Shirasu, K., and Fukuda,
1022 H. (2014). Plant GSK3 proteins regulate xylem cell differentiation downstream of TDIF-TDR
1023 signalling. Nature communications *5*, 3504.
1024 25. Saito, M., Kondo, Y., and Fukuda, H. (2018). BES1 and BZR1 Redundantly Promote Phloem
1025 and Xylem Differentiation. Plant & cell physiology *59*, 590-600.
1026 26. Brackmann, K., Qi, J., Gebert, M., Jouannet, V., Schlamp, T., Grunwald, K., Wallner, E.S.,
1027 Novikova, D.D., Levitsky, V.G., Agusti, J., et al. (2018). Spatial specificity of auxin responses
1028 coordinates wood formation. Nature communications *9*, 875.
1029 27. Shi, D., Jouannet, V., Agustí, J., Kaul, V., Levitsky, V., Sanchez, P., Mironova, V.V., and Greb,
1030 T. (2020). Tissue-specific transcriptome profiling of the Arabidopsis inflorescence stem reveals
1031 local cellular signatures. The Plant Cell.
1032 28. Agustí, J., Lichtenberger, R., Schwarz, M., Nehlin, L., and Greb, T. (2011). Characterization of
1033 Transcriptome Remodeling during Cambium Formation Identifies MOL1 and RUL1 as
1034 Opposing Regulators of Secondary Growth. PLoS genetics *7*, e1001312.
1035 29. Gursanscky, N., Jouannet, V., Grünwald, K., Sanchez, P., Laaber-Schwarz, M., and Greb, T.
1036 (2016). *MOL1* is required for cambium homeostasis in Arabidopsis. The Plant journal : for cell
1037 and molecular biology *86*, 210-220.
1038 30. Han, S., Cho, H., Noh, J., Qi, J., Jung, H.J., Nam, H., Lee, S., Hwang, D., Greb, T., and
1039 Hwang, I. (2018). BIL1-mediated MP phosphorylation integrates PXY and cytokinin signalling
1040 in secondary growth. Nature plants *4*, 605-614.
1041 31. Merks, R.M.H., and Glazier, J.A. (2005). A cell-centered approach to developmental biology.
1042 Physica A *352*, 113-130.
1043 32. Merks, R.M.H., Guravage, M., Inze, D., and Beemster, G.T. (2011). VirtualLeaf: an open-
1044 source framework for cell-based modeling of plant tissue growth and development. Plant
1045 physiology *155*, 656-666.
1046 33. Antonovici, C., Peerdeman, G.Y., Wolff, H.B., and Merks, R.M.H. (2022). Modeling Plant
1047 Tissue Development Using VirtualLeaf. In Plant Systems Biology. (Springer), pp. 165-198.
1048 34. Wolpert, L. (1969). Positional information and the spatial pattern of cellular differentiation.
1049 Journal of theoretical biology *25*, 1-47.

1050 35. Mitsuda, N., Iwase, A., Yamamoto, H., Yoshida, M., Seki, M., Shinozaki, K., and Ohme-
1051 Takagi, M. (2007). NAC transcription factors, NST1 and NST3, are key regulators of the
1052 formation of secondary walls in woody tissues of Arabidopsis. Plant Cell *19*, 270-280.
1053 36. Taylor, N.G., Howells, R.M., Huttly, A.K., Vickers, K., and Turner, S.R. (2003). Interactions
1054 among three distinct CesA proteins essential for cellulose synthesis. Proceedings of the
1055 National Academy of Sciences of the United States of America *100*, 1450-1455.
1056 37. Smith, R.A., Schuetz, M., Roach, M., Mansfield, S.D., Ellis, B., and Samuels, L. (2013).
1057 Neighboring parenchyma cells contribute to Arabidopsis xylem lignification, while lignification
1058 of interfascicular fibers is cell autonomous. Plant Cell *25*, 3988-3999.
1059 38. Sankar, M., Nieminen, K., Ragni, L., Xenarios, I., and Hardtke, C.S. (2014). Automated
1060 quantitative histology reveals vascular morphodynamics during Arabidopsis hypocotyl
1061 secondary growth. Elife *3*, e01567.
1062 39. Gujas, B., Kastanaki, E., Sturchler, A., Cruz, T.M.D., Ruiz-Sola, M.A., Dreos, R., Eicke, S.,
1063 Truernit, E., and Rodriguez-Villalon, A. (2020). A Reservoir of Pluripotent Phloem Cells
1064 Safeguards the Linear Developmental Trajectory of Protophloem Sieve Elements. Current
1065 biology : CB *30*, 755-766.e754.
1066 40. Qian, P., Song, W., Zaizen-Iida, M., Kume, S., Wang, G., Zhang, Y., Kinoshita-Tsujimura, K.,
1067 Chai, J., and Kakimoto, T. (2022). A Dof-CLE circuit controls phloem organization. Nature
1068 plants *8*, 817-827.
1069 41. Mähönen, A.P., Higuchi, M., Tormakangas, K., Miyawaki, K., Pischke, M.S., Sussman, M.R.,
1070 Helariutta, Y., and Kakimoto, T. (2006). Cytokinins regulate a bidirectional phosphorelay
1071 network in Arabidopsis. Current biology : CB *16*, 1116-1122.
1072 42. Wallner, E.S., Tonn, N., Shi, D., Jouannet, V., and Greb, T. (2020). SUPPRESSOR OF MAX2
1073 1-LIKE 5 promotes secondary phloem formation during radial stem growth. The Plant journal :
1074 for cell and molecular biology *102*, 903-915.
1075 43. Brown, C.L. (1964). The influence of external pressure on the differentiation of cells and
1076 tissues cultured in vitro. In The formation of wood in forest trees, M. Zimmerman, ed. (New
1077 York: Academic Press), pp. 389 - 404.
1078 44. Brown, C.L., and Sax, K. (1962). The influence of pressure on the differentiation of secondary
1079 tissues. American Journal of Botany *49*, 683-691.

45. Lintilhac, P.M., and Vesecky, T.B. (1984). Stress-induced alignment of division plane in plant tissues grown in vitro. Nature *307*, 363-364.

46. Ursache, R., Andersen, T.G., Marhavý, P., and Geldner, N. (2018). A protocol for combining fluorescent proteins with histological stains for diverse cell wall components. The Plant journal : for cell and molecular biology *93*, 399-412.

47. Arnould, O., Capron, M., Ramonda, M., Laurans, F., Alméras, T., Pilate, G., and Clair, B. (2022). Mechanical characterisation of the developing cell wall layers of tension wood fibres by Atomic Force Microscopy. Peer Community Journal *2*, e39.

48. Serra, O., Mähönen, A.P., Hetherington, A.J., and Ragni, L. (2022). The Making of Plant Armor: The Periderm. Annual review of plant biology *73*, 405-432.

49. Macal, C.M., and North, M.J. (2005). Tutorial on agent-based modeling and simulation. In Proceedings of the Winter Simulation Conference, 2005., p. 14 pp.

50. Green, J.B., and Sharpe, J. (2015). Positional information and reaction-diffusion: two big ideas in developmental biology combine. Development (Cambridge, England) *142*, 1203-1211.

51. Bhalerao, R.P., and Fischer, U. (2014). Auxin gradients across wood - instructive or incidental? Physiologia plantarum *151*, 43-51.

52. Etchells, J.P., Provost, C.M., and Turner, S.R. (2012). Plant vascular cell division is maintained by an interaction between PXY and ethylene signalling. PLoS genetics *8*, e1002997.

53. Wang, N., Bagdassarian, K.S., Doherty, R.E., Kroon, J.T., Connor, K.A., Wang, X.Y., Wang, W., Jermyn, I.H., Turner, S.R., and Etchells, J.P. (2019). Organ-specific genetic interactions between paralogues of the PXY and ER receptor kinases enforce radial patterning in Arabidopsis vascular tissue. Development (Cambridge, England) *146*, dev.177105.

54. Etchells, J.P., Provost, C.M., Mishra, L., and Turner, S.R. (2013). WOX4 and WOX14 act downstream of the PXY receptor kinase to regulate plant vascular proliferation independently of any role in vascular organisation. Development (Cambridge, England) *140*, 2224-2234.

55. Bishopp, A., Help, H., El-Showk, S., Weijers, D., Scheres, B., Friml, J., Benkova, E., Mähönen, A.P., and Helariutta, Y. (2011). A mutually inhibitory interaction between auxin and cytokinin specifies vascular pattern in roots. Current biology : CB *21*, 917-926.

56. Bennett, T., Hines, G., van Rongen, M., Waldie, T., Sawchuk, M.G., Scarpella, E., Ljung, K., and Leyser, O. (2016). Connective Auxin Transport in the Shoot Facilitates Communication between Shoot Apices. PLoS biology *14*, e1002446.

57. Ibanes, M., Fabregas, N., Chory, J., and Cano-Delgado, A.I. (2009). Brassinosteroid signaling and auxin transport are required to establish the periodic pattern of Arabidopsis shoot vascular bundles. Proceedings of the National Academy of Sciences of the United States of America *106*, 13630-13635.

58. Fàbregas, N., Formosa-Jordan, P., Confraria, A., Siligato, R., Alonso, J.M., Swarup, R., Bennett, M.J., Mähönen, A.P., Caño-Delgado, A.I., and Ibañes, M. (2015). Auxin influx carriers control vascular patterning and xylem differentiation in Arabidopsis thaliana. PLoS genetics *11*, e1005183.

59. Sehr, E.M., Agustí, J., Lehner, R., Farmer, E.E., Schwarz, M., and Greb, T. (2010). Analysis of secondary growth in the Arabidopsis shoot reveals a positive role of jasmonate signalling in cambium formation. The Plant journal : for cell and molecular biology *63*, 811-822.

60. Sapala, A., Runions, A., Routier-Kierzkowska, A.L., Das Gupta, M., Hong, L., Hofhuis, H., Verger, S., Mosca, G., Li, C.B., Hay, A., et al. (2018). Why plants make puzzle cells, and how their shape emerges. Elife *7*.

61. Altartouri, B., Bidhendi, A.J., Tani, T., Suzuki, J., Conrad, C., Chebli, Y., Liu, N., Karunakaran, C., Scarcelli, G., and Geitmann, A. (2019). Pectin Chemistry and Cellulose Crystallinity Govern Pavement Cell Morphogenesis in a Multi-Step Mechanism. Plant physiology *181*, 127-141.

62. Majda, M., and Robert, S. (2018). The Role of Auxin in Cell Wall Expansion. International Journal of Molecular Sciences *19*, 951.

63. Caesar, K., Elgass, K., Chen, Z., Huppenberger, P., Witthoft, J., Schleifenbaum, F., Blatt, M.R., Oecking, C., and Harter, K. (2011). A fast brassinolide-regulated response pathway in the plasma membrane of Arabidopsis thaliana. The Plant journal : for cell and molecular biology *66*, 528-540.

64. Spicer, R., and Groover, A. (2010). Evolution of development of vascular cambia and secondary growth. New Phytol *186*, 577-592.

65. Carlquist, S. (2007). Successive Cambia Revisited: Ontogeny, Histology, Diversity, and Functional Significance. The Journal of the Torrey Botanical Society *134*, 301-332.

66. Pace, M.R., Lohmann, L.G., and Angyalossy, V. (2009). The rise and evolution of the cambial variant in Bignonieae (Bignoniaceae). Evolution & development *11*, 465-479.

67. Bhalerao, R.P., and Fischer, U. (2017). Environmental and hormonal control of cambial stem cell dynamics. Journal of experimental botany *68*, 79-87.

68. Gerttula, S., Zinkgraf, M., Muday, G.K., Lewis, D.R., Ibatullin, F.M., Brumer, H., Hart, F., Mansfield, S.D., Filkov, V., and Groover, A. (2015). Transcriptional and Hormonal Regulation of Gravitropism of Woody Stems in Populus. Plant Cell *27*, 2800-2813.

69. Agustí, J., Herold, S., Schwarz, M., Sanchez, P., Ljung, K., Dun, E.A., Brewer, P.B., Beveridge, C.A., Sieberer, T., Sehr, E.M., et al. (2011). Strigolactone signaling is required for auxin-dependent stimulation of secondary growth in plants. Proc Natl Acad Sci USA *108*, 20242-20247.

70. Wallner, E.S., Lopez-Salmeron, V., Belevich, I., Poschet, G., Jung, I., Grunwald, K., Sevilem, I., Jokitalo, E., Hell, R., Helariutta, Y., et al. (2017). Strigolactone- and Karrikin-Independent SMXL Proteins Are Central Regulators of Phloem Formation. Current biology : CB *27*, 1241-1247.

71. Sommer, C., Strähle, C., Köthe, U., and Hamprecht, F.A. (2011). ilastik: Interactive Learning and Segmentation Toolkit. In Eighth IEEE International Symposium on Biomedical Imaging (ISBI). Proceedings. pp. 230-233.

72. Merks, R.M.H., and Guravage, M.A. (2013). Building simulation models of developing plant organs using VirtualLeaf. Methods Mol Biol *959*, 333-352.

73. Wickham, H., Averick, M., Bryan, J., Chang, W., D'Agostino McGowan, L., François, R., Grolemund, G., Hayes, A., Henry, L., Hester, J., et al. (2019). Welcome to the tidyverse. Journal of Open Source Software *4*, 1686.

74. Davison, A.C., and Hinkley, D.V. (1997). Bootstrap Methods and Their Applications, (Cambridge: Cambridge University Press).

75. Canty, A., and Ripley, B.D. (2020). boot: Bootstrap R (S-Plus) Functions. R package version *1*, 3-25.

76. Schindelin, J., Arganda-Carreras, I., Frise, E., Kaynig, V., Longair, M., Pietzsch, T., Preibisch, S., Rueden, C., Saalfeld, S., Schmid, B., et al. (2012). Fiji: an open-source platform for biological-image analysis. Nat Methods *9*, 676-682.

1170

1171

Figure legends

Figure 1. Generation of the initial model.

(A) Tissue template used to run VirtualLeaf simulations. Phloem* is depicted in purple, xylem* in red. Cambium cells* are colored according to their levels of PXY* and PXY-active*. Cambium* is colored in blue due to the initial level of PXY*. Color legend on the right applies to A and C.

(B) Schematic representation of the biochemical model. Reactions that occur in all cell types* are drawn in black. Reactions only occurring in the phloem* are depicted in purple, reactions specific to the cambium* are in blue. Crossed circles represent production or degradation of molecules.

(C) Output of simulation using Model 1.

(D) Visualization of cell division rates* within the output shown in (C). Dividing cells* are marked by red color fading over time.

(E) Visualization of CLE41* levels within the output shown in (C).

(F) Sorting cells* within the output shown in (C) into bins based on how far their centers are from the center of the hypocotyl*. Different colors represent different bins.

(G) Visualization of the relative chemical levels and division rates in different bins shown in (F) averaged over n=10 simulations of Model 1. Each chemical's bin concentration is first expressed as a percentage of the maximum bin value of the chemical and then averaged over all simulations. The colored area indicates the range between minimum and maximum value of the relative chemical concentration. Bin colors along the x-axis correspond to the colors of bins in (F). The shading represents the range between minimal and maximal values during simulations.

Figure 2. Implementing phloem formation into the model.

(A) Cross-section of a wild type hypocotyl expressing *PXYpro:CFP* (blue) and *SMXL5pro:YFP* (green). Cell walls are stained by Direct Red 23, mainly visualizing xylem (red). Only a sector of the hypocotyl is shown with the center on the left. Scale bar: 100 µm. An image version for color-blind readers is provided in Figure 2—figure supplement 1.

(B) Visualization of cell division rates* within the output shown in (C and E). Dividing cells* are marked by red color fading over time.

(C) Sorting cells* within the output shown in (B and E) into bins.

(D) Visualization of the average relative chemical levels* and division rates* in different bins of repeated simulations of Model 2A (n=10). Bin label colors along the x-axis correspond to the colors of bins shown in (C). The shading represents the range between minimal and maximal values during simulations.

(E) Output of simulation using Model 2A. Unlike Model 1 (Figure 1C), Model 2A produces new phloem cells*.

Figure 3. Comparing the effect of perturbing cambium activity in the model and in plants.

(A) Cross-section of a hypocotyl carrying *PXYpro:CFP* (blue), *SMXL5pro:YFP* (green) markers, and the *IRX3pro:CLE41* transgene. Cell walls are stained by Direct Red 23 visualizing mostly xylem (red). Arrowheads point to proximal hypocotyl regions where *SMXL5pro:YFP* activity is found. Arrows indicate distal regions with *SMXL5pro:YFP* activity. Cell walls are stained by Direct Red 23 visualizing mostly xylem (red). Only a quarter of the hypocotyl is shown with the center in the upper left corner. Scale bar: 100 µm. An image version for color-blind readers is provided in Figure 2—figure supplement 1.

(B) First frames of Model 2B simulations. Due to the expression of CLE41* by xylem cells*, high levels of PXY-active* are generated around xylem cells* already at this early stage. Legend in B indicates color code in B, C, D, F.

(C) Intermediate frames of Model 2B simulations. Newly formed xylem cells* express CLE41* and produce high levels of PXY-active* next to them (white arrowheads).

(D) The final result of Model 2B simulations. Zones of PXY* (blue) and PXY-active*(green) are intermixed, xylem cells* are scattered, and phloem cells* are present in proximal areas of the hypocotyl*.

(E) Cross-section of a *pxy* mutant hypocotyl carrying *PXYpro:CFP* (blue) and *SMXL5pro:YFP* (green) markers, stained by Direct Red 23 (red). The xylem shows a ray-like structure. Only a quarter of the hypocotyl is shown with the center in the upper left corner. Scale bar: 100 µm. An image version for color-blind readers is provided in Figure 2—figure supplement 1.

(F) Final result of Model 2D simulations. Reducing PXY* levels leads to similar results as produced by Model 1 (Figure 1C) where only xylem* is produced.

(G, H) Comparison of histological cross-sections of a wild type (G) and a *pxy* (H) mutant hypocotyl, including cell type classification produced by ilastik. The ilastik classifier module was trained to identify xylem vessels (red), fibers (green), and parenchyma (purple), unclassified objects are shown in yellow.

(I) Comparison of the number of xylem vessels, fibers and parenchyma cells found in wild type (blue) and *pxy* mutants (purple). Welch's t test was performed comparing wild-type and *pxy* mutants for the different cell types (n = 11-12). ***$p < 0.0001$, *$p < 0.05$. Lines indicate means with a 95 % confidence interval.

Figure 4. An extended model for simulating genetic perturbations of cambium activity.

(A) Regulatory network proposed based on experimental observations.

(B) Result of the simulation run for Model 3A. This model implements the network interactions described in (A). Color coding at the bottom of Figure 4.

(C) Outline of cell bins for the results of Model 3A, as shown in (B).

(D) Visualization of the relative levels of chemicals* and division rates* in different bins. Bin colors along the x-axis correspond to the bin colors in (C). The shading represents the range between minimal and maximal values during simulations.

(E) Output of Model 3B simulation. Ectopic CLE41* expression was achieved by letting xylem cells* produce CLE41*.

(F) Output of Model 3C. Simulation of the *pxy* mutant was achieved by removing the stimulation of DF* production by PXY* and hence by removing the effect of PXY* on cell division and cambium* subdomain patterning. Because of the network structure, PXY* can be eliminated from Model 3 without letting the model collapse (Figure 3F) but reproducing the *pxy* mutant phenotype observed in adult hypocotyls (Figure 4E). Be aware that cell* proliferation is generally impaired under these conditions reducing overall template growth*. Because the final output covers the same image area, cell size seems to be enlarged which, however, is not the case.

(G) Estimated tissue ratios for five identified parameter sets compared to experimental values ('data') found for wild type hypocotyls 20 days after germination [38] and compared to the final model output before the automated parameter search ('Model 3A') and the implementation of experimentally determined cell wall thickness for xylem* and phloem*.

Figure 5. Effect of xylem cell wall stiffness* on the radiality of cambium-derived cell lineages*.

(A) Final output of Model 4 and parameter set 1.

(B) Visualization of the relative levels of chemicals* and division rates* in different bins. Bin colors along the x-axis correspond to the different bins similarly as in Figure 4C. The shading represents the range between minimal and maximal values during simulations.

(C, D) Simulation outputs at increasing values of xylem stiffness* (C) and epidermis stiffness* (D) with the ratio of stiffness* vs. experimentally determined xylem stiffness indicated at the right bottom corner of each example. All the simulations had the same starting conditions and ran for the same amount of simulated time. At the bottom, there is a magnification of the right region shown in the pictures above, respectively.

(E, F) Examples of the relationship between R^2 and the geometry of proliferation trajectories (grey arrows) for two different R^2 values; dots are cell* centroids, lines represent division* events.

(G, H) Fraction of median relative amount of lineages whose R^2 falls within a specific range for ten simulations in each condition (n≥70 lineages per simulation) at different xylem stiffness* (G) and epidermis stiffness* (H) regimes. In case of significant difference among medians, assessed with Kruskal-Wallis (KW significance is $p < 2.6$ E-3 for (0, 0.25) interval and $p < 9.17e-7$ for the (0.75,1) interval), the pairwise difference between medians was tested post hoc applying the Dunn test. The post hoc results are reported in each box as letters; medians sharing the same letter or do not display a letter at all do not differ significantly.

Figure 3—figure supplement 1. First example revealing the dynamics of *PXYpro:CFP/SMXL5pro:YFP* activities during radial hypocotyl growth in wild type, *IRX3pro:CLE41* and *pxy* plants.

(A-D) *PXYpro:CFP* (blue) and *SMXL5pro:YFP* (green) activities at different stages of wild type hypocotyl development from young (A) to old (D).
(E-H) *PXYpro:CFP* (blue) and *SMXL5pro:YFP* (green) activities at different stages of hypocotyl development in *IRX3pro:CLE41* plants from young (A) to old (D).
(I-L) *PXYpro:CFP* (blue) and *SMXL5pro:YFP* (green) activities at different stages of hypocotyl development in *pxy* mutants from young (A) to old (D).
Sections are stained by Direct Red 23 (red). Scale bars: 100 µm. Note that pictures D, H and L are also depicted in Figure 2 and Figure 3. A version of this figure for color-blind readers is provided in Figure 3—figure supplement 3.

Figure 3—figure supplement 2. Second example revealing the dynamics of *PXYpro:CFP/SMXL5pro:YFP* activities during radial hypocotyl growth in wild type, *IRX3pro:CLE41* and *pxy* plants.

(A-D) *PXYpro:CFP* (blue) and *SMXL5pro:YFP* (green) activities at different stages of wild type hypocotyl development from young (A) to old (D).
(E-H) *PXYpro:CFP* (blue) and *SMXL5pro:YFP* (green) activities at different stages of hypocotyl development in *IRX3pro:CLE41* plants from young (A) to old (D).
(I-L) *PXYpro:CFP* (blue) and *SMXL5pro:YFP* (green) activities at different stages of hypocotyl development in *pxy* mutants from young (A) to old (D).
Sections were stained by Direct Red 23 (red). Scale bars: 100 µm. A version of this figure for color-blind readers is provided in Figure 3—figure supplement 4.

Figure 3—figure supplement 3. First example revealing the dynamics of *PXYpro:CFP/SMXL5pro:YFP* activities during radial hypocotyl growth in wild type, *IRX3pro:CLE41* and *pxy* plants (color-blind mode).

(A-D) *PXYpro:CFP* (blue) and *SMXL5pro:YFP* (green) activities at different stages of wild type hypocotyl development from young (A) to old (D).
(E-H) *PXYpro:CFP* (blue) and *SMXL5pro:YFP* (green) activities at different stages of hypocotyl development in *IRX3pro:CLE41* plants from young (A) to old (D).
(I-L) *PXYpro:CFP* (blue) and *SMXL5pro:YFP* (green) activities at different stages of hypocotyl development in *pxy* mutants from young (A) to old (D).
Sections are stained by Direct Red 23 (red). Scale bars: 100 μm. Note that pictures D, H and L are also depicted in Figure 2 and Figure 3.

Figure 3—figure supplement 4. Second example revealing the dynamics of *PXYpro:CFP/SMXL5pro:YFP* activities during radial hypocotyl growth in wild type, *IRX3pro:CLE41* and *pxy* plants (color-blind mode).

(A-D) *PXYpro:CFP* (blue) and *SMXL5pro:YFP* (green) activities at different stages of wild type hypocotyl development from young (A) to old (D).
(E-H) *PXYpro:CFP* (blue) and *SMXL5pro:YFP* (green) activities at different stages of hypocotyl development in *IRX3pro:CLE41* plants from young (A) to old (D).
(I-L) *PXYpro:CFP* (blue) and *SMXL5pro:YFP* (green) activities at different stages of hypocotyl development in *pxy* mutants from young (A) to old (D).
Sections were stained by Direct Red 23 (red). Scale bars: 100 μm.

Figure 3—figure supplement 5. Close-up revealing the dynamics of *PXYpro:CFP/SMXL5pro:YFP* activities in hypocotyls in wild type and *pxy* plants.

(A-C) Three examples showing *PXYpro:CFP* (top, bottom, in magenta) and *SMXL5pro:YFP* (middle, bottom, in green) activities in the cambium zone of wild type plants. Scale bar in A: 20 µm. Same magnification in A-F.

(D-F) Three examples showing *PXYpro:CFP* (top, bottom, in magenta) and *SMXL5pro:YFP* (middle, bottom, in green) activities in the cambium zone of *pxy* mutants. Note that Direct Red 23 staining (in grey) is only shown in top and middle imageds but not in 'merged' images at the bottom. Shown are late stages as depicted in Figure 3—figure supplement 1C, K and Figure 3—figure supplement 2C, K.

Figure 3—figure supplement 6: Overview and magnifications of sections used for cell type classification shown in Fig. 3.

Original toluidine-stained cross sections (A, D), cross section with cell type-classifications (B, E) and magnifications of regions indicated by black rectangles in B and E (C, F) for wild type (A, B, C) and *pxy* mutants (D, E, F) are shown. Cell type classification was exclusively performed in the xylem area.

Figure 4—figure supplement 1. Overview of cell types*, regulatory interactions and expression* profiles in Model 3. Schemes include representations for Model 3B and C. Color code shown at the bottom of the figure.

Figure 4—figure supplement 2. Determination of cell wall thickness across the radial sequence of hypocotyl tissues.

(A) Cross section of a 4.5 week-old plant stained by Direct Red 23. Radius and circumference used by the 'Radial Profile' function of the Fiji image analysis tool [76] are indicated. Note that the function uses the whole circle area for analysis.

(B) Plot of six Direct Red 23-stained cross sections analyzed by the 'Radial Profile' function of Fiji. Staining intensity and radius were normalized to 1 by dividing obtained values by maximum values within respective sample data sets.

(C) Average intensity profile of Direct Red 23 staining for three sections as shown in Figure 2A determined by the 'Radial Profile' function of Fiji. Staining intensity and radius were normalized to 1 by dividing obtained values by maximum values within respective sample data sets.

Figure 4—figure supplement 3. Behavior of the different model parameterizations (Model 4:2-5).

(A) Overview of parameter values of the different parameter sets. Shown are the relative values of the estimated parameter compared to the original parameter values. Horizontal lines indicate the lower (1/3) and upper (3-fold) boundary (grey) as well as the original parameter value (blue).

(B) Behavior of parameter sets 2-5. Shown is the final output of the simulation, the tissue* sorted into bins as well as the average chemical concentration* per bin (for n=10 simulations). The shading represents the range between minimal and maximal values during simulations.

Figure 5—figure supplement 1. Distribution of cell* properties under different xylem 'stiffness' regimes.

(A) Cell* size in arbitrary units

(B) Major axis lengths of cells* in arbitrary units

(C) Numbers of nodes (vertexes) per cell*

(D) Number of cells*

among cell types and stiffness values for n=30 simulations under each stiffness regime. The blue color highlights the simulation at the experimentally determined thickness/stiffness value. The x-axis indicates values of xylem stiffness as the ratio of xylem stiffness* vs. experimentally determined thickness/stiffness. A slight horizontal displacement of points has been added to enhance visualization. Values for individual cells* found in all 30 simulations are displayed in A-C, whereas numbers of cells* in each cell type* for each one of the 30 simulations are shown in D.

Figure 5—figure supplement 2. Distribution of cell* properties under different tissue boundary (=epidermis*) 'stiffness' regimes

(A) Cell* size in arbitrary units

(B) Major axis lengths of cells* in arbitrary units

(C) Numbers of nodes (vertexes) per cell*

(D) Number of cells*

among cell types and stiffness values for n=30 simulations under each stiffness regime. The blue color highlights the simulation running at normal stiffness level; the x-axis indicates values of the relative perimeter stiffness as the fold-change compared to the standard parameters. A slight horizontal displacement of points has been added to enhance visualization. Values for individual cells* found in all 30 simulations are displayed in A-C, whereas numbers of cells* in each cell type* for each one of the 30 simulations are shown in D.

Figure 5—figure supplement 3. Fraction of median relative amount of cell lineages for parameter sets 2-5.

(**A**) With increasing xylem* 'stiffness'

(B) With increasing epidermis* ‘stiffness’

Figure 5—figure supplement 4. Fraction of median relative amount of cell lineages at different parameters governing cell wall* dynamics.

The model parameters cell walls’ target length and yielding threshold were varied by +/-50% and the behavior at different cell wall stiffness values simulated. The statistical analysis was done as described before for Figure 5 for n=10 simulations each and n≥70 cell lineages per simulation.

Description of the VirtualLeaf simulations

VirtualLeaf allows for models to combine tissue dynamics, cell behavior dynamics and biochemical networks that span between cells. The different modeling scales are simulated iteratively: During each simulation step, the tissue dynamics are simulated first using Monte Carlo simulations until a stable energy of the Hamiltonian is reached. Only then are the biological rules applied, with cell division occurring last in order to prevent new cells from interfering with the simulations.

For a detailed description of the simulation process see Merks et al. (2011, 2013) and Antonovici et al. (2022). Here, we include a brief overview of tissue simulations in VirtualLeaf and outline the changes we made for model 4 as well as the biological rules of the different cambium model versions. The base VirtualLeaf source code is available for download from https://github.com/rmerks/VirtualLeaf2021. The custom version of VirtualLeaf that we built for this analysis as well as the models described in this paper are available at https://github.com/thomasgreb/Lebovka-et-al_cambium-models.

Tissue simulations

The tissue dynamics are simulated using Monte Carlo simulation dynamics. Briefly, VirtualLeaf attempts to move all nodes of the model in a random order. A Hamiltonian operator is used to assess the energy of the system at both the old and the new position of the node. The movement of nodes is accepted if it minimizes the energy of the system. This operator considers both the cells' compression and the resistance of the cell wall elements to being stretched or compressed (Merks et al. 2011):

$$H = \lambda_A \sum_i (a(i) - A_T(i))^2 - \lambda_M \sum_j (l(j) - L_T(j))^2$$

with λ_A as the cell's resistance to compression or expansion, λ_M the spring constant for the cell wall elements, A_T and L_T are the cell's target area and the cell wall's target length, respectively, with $a(i)$ representing the current cell area and $l(j)$ the current wall length. For models 1-3C the standard implementation of the Hamiltonian operator was used.

Cellular growth is implemented in VirtualLeaf as an increase in the cells' target areas. Until the maximal cell size is reached, a cell's target area $A_T(i)$ is increased by a fixed amount in each simulation step. This results in increasing the contribution of the area compression to the Hamiltonian operator

For model 4 the calculation of the Hamiltonian was refined to include a more detailed definition of the second term for the calculation of the cell wall component of the system's energetic state:

$$\lambda_M \sum \frac{(\lambda_{L1} + \lambda_{L2})}{2} (l(j) - L_T(j))^2$$

Here, $\lambda_{L1,2}$ are cell specific spring constants for the cells that share each specific wall element j. Specifically, λ_{L1} and λ_{L2} are relative contributions to the stiffness of the joint cell wall, where each contribution represents the half of the cell wall secreted by that particular cell. To make the cell wall module compatible with earlier VirtualLeaf models, the default value for λ_L is set to "1" such that the expanded calculations result in a multiplication by "1" and do not affect the calculations of the Hamiltonian. The changes to the code in our custom version of VirtualLeaf are marked by a comment "Lebovka et al" at the respective lines of code.

Take the cellular layout of figure 1 as exemplary situation, where node 5 is being moved. During the calculations of the cell wall elements, there are three walls to consider: between nodes 5 and 6, between 5 and 7, and between 5 and 4. As indicated by the arrows, each cell wall will be considered twice during the calculations for the move of node 5: The cell wall between node 4 and node 5 will be called once for cell 1 and once for cell 3, taking into account the specific cell wall thickness specific for each cell.

Altogether, this allows a cell type specific representation of the stiffness of the cell wall elements and therefore a more realistic representation of tissue structure such as an increased cell wall thickness and stability of xylem cells.

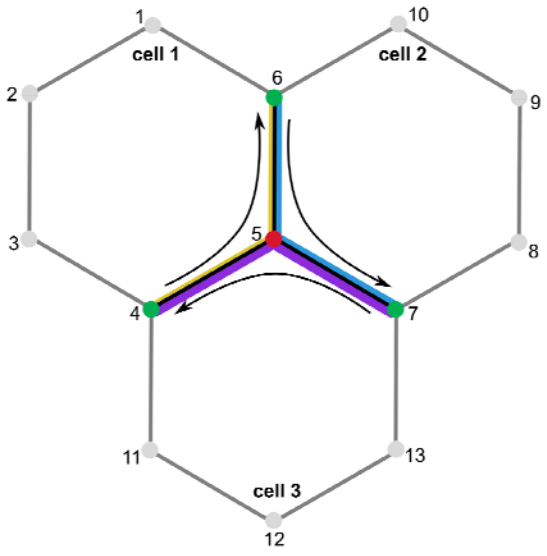

Figure 1 - Cell wall calculations during node movement. Node 5 is moved to a new position. During calculations the change in wall elements between nodes 5 and 6, 5 and 7 as well as 5 and 4 is considered. The cell specific stiffness of the wall elements is indicated by the thickness of the colored lines – yellow for cell 1, blue for cell 2 and purple for cell 3.

As all the nodes are moved in a random order, this may cause some variation on the tissue layout between simulations. As a consequence, the application of cell behavior rules can vary as well between simulation runs, e.g. as cells divide over the longest axis and not in a

predetermined direction. To account for these variations between simulations, we simulated each model, each parameter set and each thickness regime at least ten times.

Cambium Models

Models in VirtualLeaf comprise four different files: (1) the project file, (2) the model header file, (3) the C++ file containing the model algorithm and (4) the tissue layout. We provide these four files for the cambium models in the GitHub repository linked above. The model will further need to be included in the Model.pro file as a subdirectory by including the line "Model_folder \" as one of the entries below "SUBDIR = \".

1. Model.pro

This is a C++ project file containing the configuration settings and pathways for the necessary directories.

2. Model.h

This is a C++ header file containing a line with the following structure: "virtual QString DefaultLeafML(void) {return QString("hypo7.xml");}". The line indicates where VitualLeaf should search for an xml file that describes the structure of the tissue template (called "leaf") used for the model to run upon. In this particular example, the name of the xml template is "hypo7.xml". VirtualLeaf will go to the folder in which you installed the software and will look for this file in the subfolder "../data/leaves". In our case, a Windows machine was used. Therefore, the full path looked like this: "C:\VirtualLeaf2021-main\data\leaves" and this folder contained a file "hypo7.xml". Please note that paths will be different depending on the operating system being used.

2. Model.cpp

A C++ file containing the model algorithm to reproduce the output described in this study. Each model contains specific rules for cell behavior and biochemical equations specific to the cell types defined in the leaf.xml file. The cell behavior rules are listed in the sections *OnDivide* and *CellHousekeeping* while the biochemical model is listed in the section *CellDynamics*. Cell-to-cell transport is considered in the section *CelltoCellTransport* with reactions at cell walls having their specific section *WallDynamics*, though the latter was not used in any of the Cambium models.

2.1 Cell behavior models

All cells in the cambium models follow specific behavioral rules governing cell growth, cell division and cell differentiation (Supplementary File 2). Generally, cells grow until a maximal size is reached, unless other behavior rules are triggered. Cell division and differentiation require not only a minimal cell size but also additional conditions regarding chemical concentrations. Unless otherwise specified, all cell behavior rules are applied as long as the specific conditions are met.

2.2 Biochemical Model

Model 1 & 2

In cambium* and xylem* cells, CLE41 dynamics are a combination of the diffusion of CLE41*, the binding to PXY* and the degradation of CLE41*:

$$\frac{d}{dt}[CLE41^*] = diffusion_{CLE41} - [PXY^*] \cdot [CLE41^*] - degradation_{CLE41} \cdot [CLE41^*]$$

In phloem* cells, there is an additional term in the equation describing the production of CLE41*:

$$\frac{d}{dt}[CLE41^*] = diffusion_{CLE41} + production_{CLE41} - [PXY^*] \cdot [CLE41^*]$$

$$-degradation_{CLE41} \cdot [CLE41^*]$$

PXY* is produced in cambium* cells and negatively regulated by bound PXY*:

$$\frac{d}{dt}[PXY^*] = \frac{production_{PXY}}{(1 + suppress\ rate \cdot [PXY^*_{active}])} - [PXY^*] \cdot [CLE41^*]$$

$$-degradation_{PXY} \cdot [PXY^*]$$

In the other cell types* in turn, free PXY* is governed by CLE41* binding to PXY* as well as the degradation of the receptor:

$$\frac{d}{dt}[PXY^*] = -[PXY^*] \cdot [CLE41^*] - degradation_{PXY} \cdot [PXY^*]$$

The ODE describing the dynamics of bound PXY* is identical for all cell types*. Here, bound PXY* is produced by the association of CLE41* and PXY and later degraded:

$$\frac{d}{dt}[PXY^*_{active}] = [PXY^*] \cdot [CLE41^*] - degradation_{PXY^*_{active}} \cdot [PXY^*_{active}]$$

Model 2B

In model 2B CLE41* is also produced in xylem cells*, such that the ODE now reads as follows:

$$\frac{d}{dt}[CLE41^*] = diffusion_{CLE41} + production_{CLE41} - [PXY^*] \cdot [CLE41^*]$$

$$-degradation_{CLE41} \cdot [CLE41^*]$$

Model 2C & D

In model 2C and D the production of PXY* in cambium cells is eliminated (C) or strongly reduced (D). As such, the ODE for PXY* in model 2D is now:

$$\frac{d}{dt}[PXY^*] = \frac{0.1 \cdot production_{PXY}}{(1 + suppress\ rate \cdot [PXY^*_{active}])} - [PXY^*] \cdot [CLE41^*]$$

$$-degradation_{PXY} \cdot [PXY^*]$$

For model 2C the production term is set to “0”, fully eliminating PXY* production in cambium cells*.

Models 3 & 4

In models 3 and 4 we expanded the biochemical network to include additional chemicals suppressing PXY expression (RP*), a dedicated division factor as well as phloem derived factors promoting the division factor and suppressing phloem pole formation (PF_{div}* and PF_{pole}*, respectively). While the ODEs for CLE41*, free PXY* and bound PXY* remain mostly unchanged, we refined the ODE for PXY* to make the production of PXY* independent of PXY_{active}*:

$$\frac{d}{dt}[PXY^*] = \frac{production_{PXY}}{\left(1 + suppress\ rate \cdot \left[RP^*\right]\right)} - [PXY^*] \cdot [CLE41^*]$$

$$-degradation_{PXY} \cdot [PXY^*]$$

We also set the production rates of CLE41* to be higher in phloem poles* than in phloem parenchyma*.

The factor suppressing PXY expression (RP*) diffuses and is degraded throughout the tissue but is only produced in phloem cells. We therefore get in the following equation for phloem cells:

$$\frac{d}{dt}[RP^*] = production_{RP} + diffusion_{RP} - degradation_{RP} \cdot [RP^*]$$

In all other cell types, this ODE is simplified to include only the diffusion and degradation of RP*.

For the second phloem-derived factor, PF*, two chemicals were defined in the biochemical model on account of the different functions in the model reminiscent of different signaling components in planta: promoting the production of the division chemical reminiscent of the PEAR transcription factors (PF_{div}*) and suppressing phloem pole formation reminiscent of the CLE45/ RPK2 signaling module (PF_{pole}*). The respective ODEs for both PF_{div}* and PF_{pole}* in phloem poles* are therefore:

$$\frac{d}{dt}[PF^*_{div}] = production_{PF} + diffusion_{PF} - degradation_{PF} \cdot [PF^*_{div}]$$

$$\frac{d}{dt}\left[PF^*_{pole}\right] = production_{PF} + diffusion_{PF} - degradation_{PF} \cdot \left[PF^*_{pole}\right]$$

In all other cell types, these ODE are simplified to include only the diffusion and degradation of PF_{div}* and PF_{pole}*.

Last, we included a factor promoting the division of cambium* and phloem parenchyma* cells (DF*). Generally, the division chemical DF* is degraded in tissues:

$$\frac{d}{dt}[DF^*] = diffusion_{DF} - degradation_{DF} \cdot [DF^*]$$

149 Only, in phloem parenchyma* and cambium* cells this chemical is also produced:

$$\frac{d}{dt}[DF^*] = \frac{production_{DF} \cdot ([PF^*] + 100 * [PXY^*_{active}])}{K + [PF^*] + 100 * [PXY^*_{active}]} + diffusion_{DF}$$

$$-degradation_{DF} \cdot [DF^*]$$

150 **Model 3B**

151 In model 3B CLE41* is also produced in xylem cells*, such that the ODE now reads as
152 follows:

$$\frac{d}{dt}[CLE41^*] = diffusion_{CLE41} + production_{CLE41} - [PXY^*] \cdot [CLE41^*]$$

153 $$-degradation_{CLE41} \cdot [CLE41^*]$$

154

155 **Model 3C**

156 In model 3C, the implementation of the *pxy* mutant was two-fold, as we needed PXY* in the
157 model for the positional information during xylem cell* differentiation. First, the production of
158 PXY^*_{active} was set to zero. And second, the DF* production only depended on DF*:

159 $$\frac{d}{dt}[DF^*] = \frac{production_{DF} \cdot ([PF^*])}{K + [PF^*]} + diffusion_{DF} - degradation_{DF} \cdot [DF^*]$$

160

161 **Diffusion**

162 Generally, we defined the diffusion flux phi according to Fick's law, i.e. based on the
163 concentrations of neighboring cells and the length of the shared cell wall element

164 $$phi = diffusion\ rate \cdot length_{wall\ element} \cdot (concentration_{cell\ 2} - concentration_{cell\ 1}),$$

so that the change in cell 1 is equal to phi and the change in cell 2 is equal to $-phi$. To ensure mass conservation, we included an additional factor correcting for different cell sizes:

$$\frac{d(concentration_{cell\,1})}{dt} = \frac{area_{cell\,2}}{area_{total}} \cdot phi$$

$$\frac{d(concentration_{cell\,2})}{dt} = -\frac{area_{cell\,1}}{area_{total}} \cdot phi$$

With $area_{total}$ defined as the sum of the sizes of cell 1 and cell 2.

In model 1 only CLE41 diffuses between cells with no restrictions regarding to cell types. In models 3 and 4 we also considered the diffusion of RP*, PF_{div}*, PF_{pole}* and DF*, all of which were calculated according to the equation above and without restrictions regarding to cell types.

3. Leaf.xml

A file containing the description of a tissue template as described before (Merks *et al.* 2011). The software uses this file to construct a tissue template and to run a given model.

In order to run or modify a provided model, follow the following instructions.

a. Create a new model with the desired name (e.g. “my_cool_model”) as described (Merks *et al.* 2011).

b. After a new model was created, there should be a folder “../src/Models/my_cool_model” in your VirtualLeaf folder. In our case, the full path looked like this: “C:\VirtualLeaf2021-main\src\Models\ my_cool_model”.

c. In your “../src/Models/my_cool_model” folder locate “my_cool_model.h” and “my_cool_model.cpp” files. Using a text editor replace the content of those files by the

content of the respective files from the model you are interested in (files provided in this paper are called “Model1.h” and “Model1.cpp”). Please note that you should only replace the content of the files and not the files themselves. After you have completed this step, your files should still be named “my_cool_model.h” and “my_cool_model.cpp”.

d. Open the files “my_cool_model.h” and “my_cool_model.cpp” using a text editor and replace every instance of “Model1” by “my_cool_model” in the text. Save the changes.

e. Locate the “../data/leaves” folder and add the provided xml file defining the tissue template (in our case, the tissue template is called “hypo7.xml’). The resulting full path to the file had the following structure in our case: “C:\VirtualLeaf2021-Main\data\leaves\hypo7.xml”.

f. Compile the model as described (Merks *et al.* 2011, Antonovici *et al.* 2022). Please note that each time you introduce changes into the code, you should recompile the model and re-start VirtualLeaf.

g. Now you can run VirtualLeaf. Go to the “../bin’ folder and run the “VirtualLeaf” file. In our case the full path looked like this: “C:\VirtualLeaf2021-main\bin\VirtualLeaf ”.

The new model will appear under the “Models” section with the corresponding name. Please note that the name of the model that will be shown is not the same as “my_cool_model”. Instead, it will show whichever name was indicated in the “my_cool_model.cpp” file in this line: // specify the name of your model here; return QString("Model 1 - pxy only")”. In this case, there will be a new model called “Model 1 - pxy only” in the VirtualLeaf folder under the “Models” section.

References

Merks, R. M. H., Guravage, M., Inze, D., & Beemster, G. T. S. (2011). VirtualLeaf: An Open-Source Framework for Cell-Based Modeling of Plant Tissue Growth and Development. *Plant Physiology*, *155*(2), 656–666. https://doi.org/10.1104/pp.110.167619

Merks, R.M.H., and Guravage, M.A. (2013). Building simulation models of developing plant organs using VirtualLeaf. Methods Mol Biol *959*, 333-352.

Antonovici, C. C., Peerdeman, G. Y., Wolff, H. B., & Merks, R. M. H. (2022). Modeling Plant Tissue Development Using VirtualLeaf. In *Plant Systems Biology* (pp. 165-198). Humana, New York, NY.

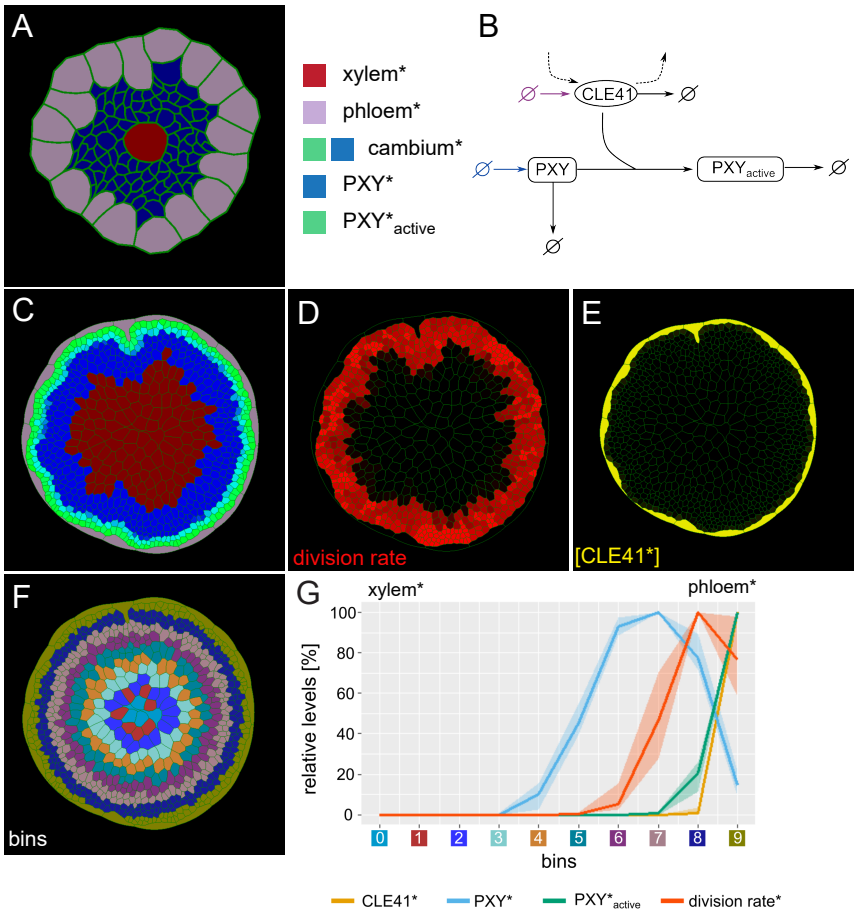

Figure 1. Generation of the initial model.
(A) Tissue template used to run VirtualLeaf simulations. Phloem* is depicted in purple, xylem* in red. Cambium cells* are colored according to their levels of PXY* and PXY-active*. Cambium* is colored in blue due to the initial level of PXY*. Color legend on the right applies to A and C.
(B) Schematic representation of the biochemical model. Reactions that occur in all cell types* are drawn in black. Reactions only occurring in the phloem* are depicted in purple, reactions specific to the cambium* are in blue. Crossed circles represent production or degradation of molecules.
(C) Output of simulation using Model 1.
(D) Visualization of cell division rates* within the output shown in (C). Dividing cells* are marked by red color fading over time.
(E) Visualization of CLE41* levels within the output shown in (C).
(F) Sorting cells* within the output shown in (C) into bins based on how far their centers are from the center of the hypocotyl*. Different colors represent different bins.
(G) Visualization of the relative chemical levels and division rates in different bins shown in (F) averaged over n=10 simulations of Model 1. Each chemical's bin average is calculated and then expressed as a percentage of the maximum bin value of the chemical. Bin colors along the x-axis correspond to the colors of bins in (F).

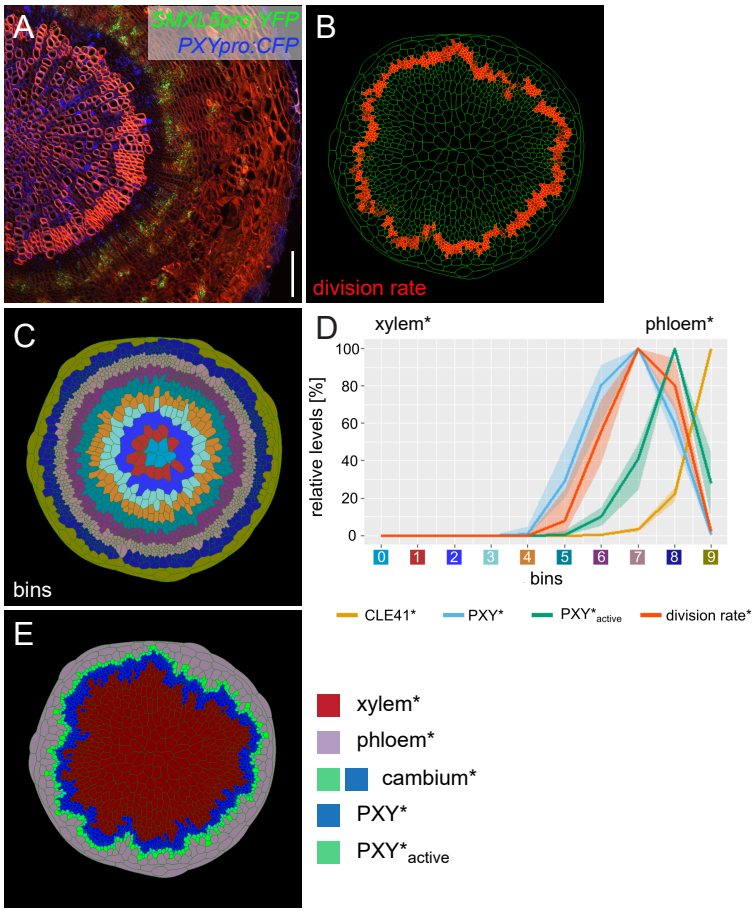

Figure 2. Implementing phloem formation into the model.
(A) Cross-section of a wild type hypocotyl expressing *PXYpro:CFP* (blue) and *SMXL5pro:YFP* (green). Cell walls are stained by Direct Red 23, mainly visualizing xylem (red). Only a sector of the hypocotyl is shown with the center on the left. Scale bar: 100 µm.
(B) Visualization of cell division rates* within the output shown in (C and E). Dividing cells* are marked by red color fading over time.
(C) Sorting cells* within the output shown in (B and E) into bins.
(D) Visualization of the average relative chemical levels* and division rates* in different bins of repeated simulations of Model 2A (n=10). Bin label colors along the x-axis correspond to the colors of bins shown in (C).
(E) Output of simulation using Model 2A. Unlike Model 1 (Figure 1C), Model 2A produces new phloem cells*.

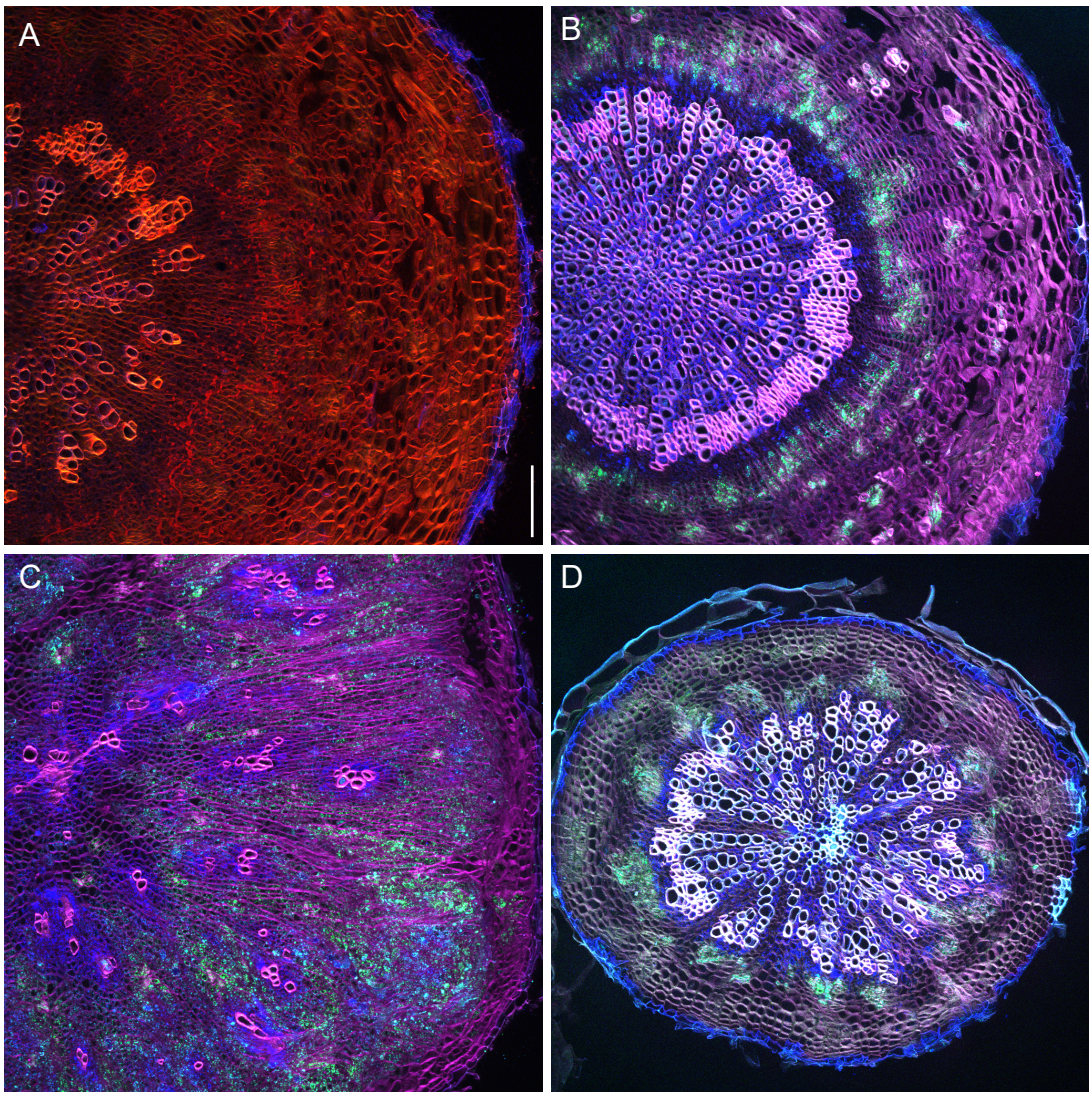

Figure 2—figure supplement 1.
(A) A hypocotyl cross section from a wild type plant not carrying any transgene, which was stained and imaged in the same way as for example the section shown in Figure 2A. The signal detected in the outermost cell layer applying the microscope settings used for detecting *PXYpro:CFP* activity (in blue) originates from autofluorescence possibly due to suberin deposition in that cell layer. Scale bar: 100 µm.
(B-D) Images shown in Figures 2A, 3A and 3E, respectively, in which the red colour was replaced by magenta.

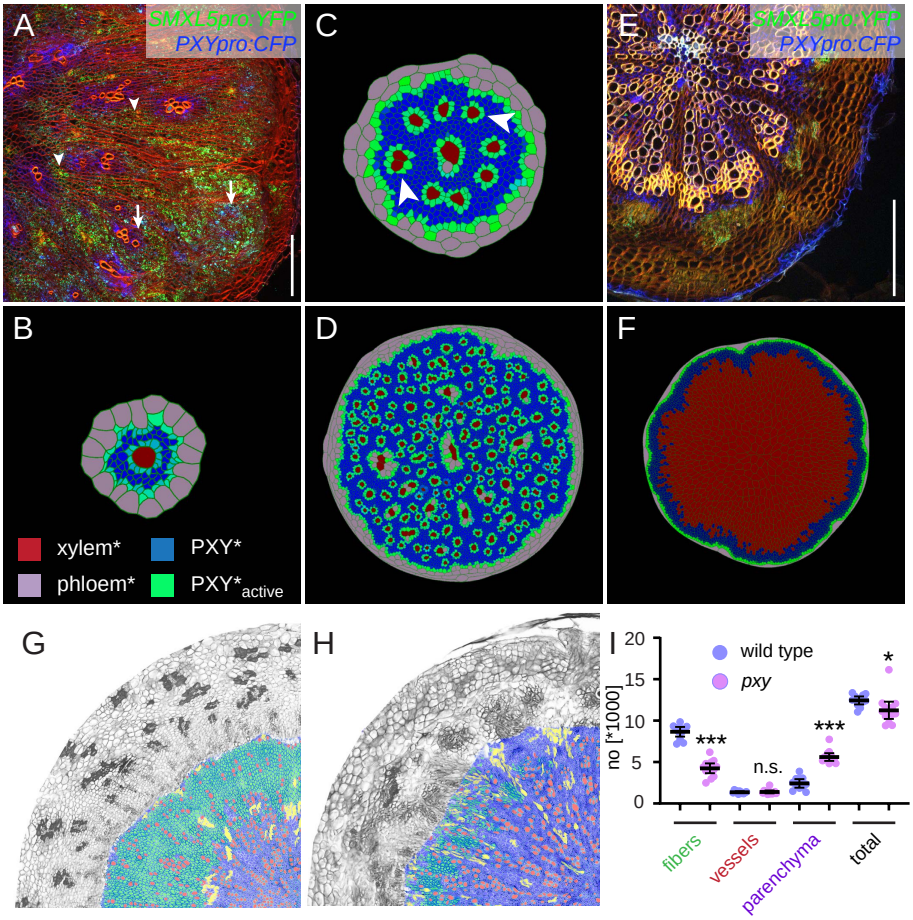

Figure 3. Comparing the effect of perturbing cambium activity in the model and in plants.
(A) Cross-section of a hypocotyl carrying *PXYpro:CFP* (blue), *SMXL5pro:YFP* (green) markers, and the *IRX3pro:CLE41* transgene. Cell walls are stained by Direct Red 23 visualizing mostly xylem (red). Arrowheads point to proximal hypocotyl regions where *SMXL5pro:YFP* activity is found. Arrows indicate distal regions with *SMXL5pro:YFP* activity. Cell walls are stained by Direct Red 23 visualizing mostly xylem (red). Only a quarter of the hypocotyl is shown with the center in the upper left corner. Scale bar: 100 µm.
(B) First frames of Model 2B simulations. Due to the expression of CLE41* by xylem cells*, high levels of PXY-active* are generated around xylem cells* already at this early stage. Legend in B indicates color code in B, C, D, F.
(C) Intermediate frames of Model 2B simulations. Newly formed xylem cells* express CLE41* and produce high levels of PXY-active* next to them (white arrowheads).
(D) The final result of Model 2B simulations. Zones of PXY* (blue) and PXY-active*(green) are intermixed, xylem cells* are scattered, and phloem cells* are present in proximal areas of the hypocotyl*.
(E) Cross-section of a *pxy* mutant hypocotyl carrying *PXYpro:CFP* (blue) and *SMXL5pro:YFP* (green) markers, stained by Direct Red 23 (red). The xylem shows a ray-like structure. Only a quarter of the hypocotyl is shown with the center in the upper left corner. Scale bar: 100 µm.
(F) Final result of Model 2D simulations. Reducing PXY* levels leads to similar results as produced by Model 1 (Figure 1C) where only xylem* is produced.
(G, H) Comparison of histological cross-sections of a wild type (G) and a pxy (H) mutant hypocotyl, including cell type classification produced by ilastik. The ilastik classifier module was trained to identify xylem vessels (red), fibers (green), and parenchyma (purple), unclassified objects are shown in yellow.
(I) Comparison of the number of xylem vessels, fibers and parenchyma cells found in wild type (blue) and *pxy* mutants (purple). Welch's t test was performed comparing wild-type and *pxy* mutants for the different cell types (n = 11-13). ***$p < 0.0001$, *$p < 0.05$. Lines indicate means with a 95 % confidence interval. 11-12 plants each for wild type and *pxy* mutants were compared.

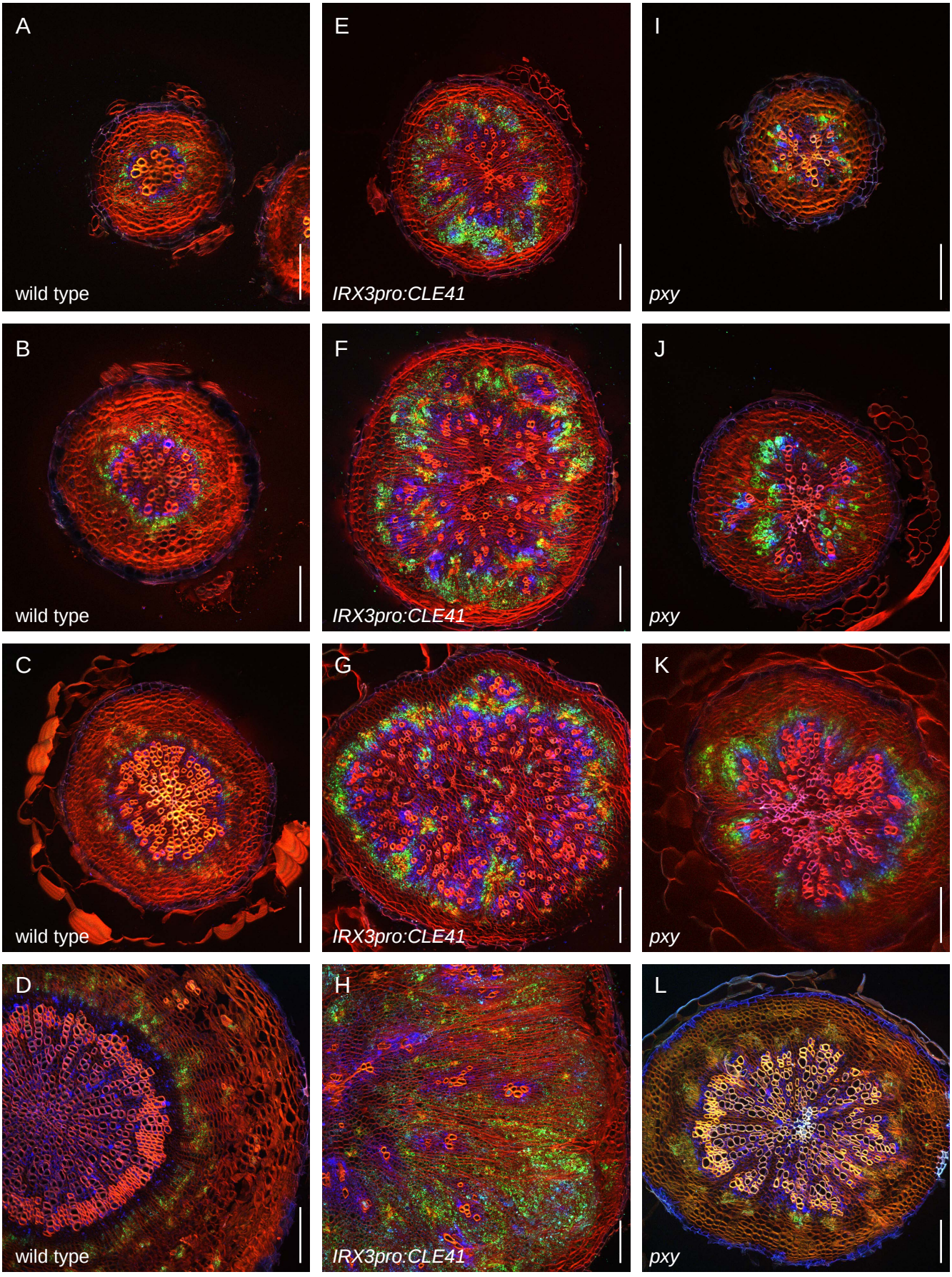

Figure 3—figure supplement 1. First example revealing the dynamics of *PXYpro:CFP/SMXL5pro:YFP* activities during radial hypocotyl growth in wild type, *IRX3pro:CLE41* and *pxy* plants.
(A-D) *PXYpro:CFP* (blue) and *SMXL5pro:YFP* (green) activities at different stages of wild type hypocotyl development from young (A) to old (D). **(E-H)** *PXYpro:CFP* (blue) and *SMXL5pro:YFP* (green) activities at different stages of hypocotyl development in *IRX3pro:CLE41* plants from young (E) to old (H). **(I-L)** *PXYpro:CFP* (blue) and *SMXL5pro:YFP* (green) activities at different stages of hypocotyl development in *pxy* mutants from young (I) to old (L). Sections are stained by Direct Red 23 (red). Scale bars: 100 µm. Note that pictures D, H and L are also depicted in Figure 2 and Figure 3. A version of this figure for color-blind readers is provided in Figure 3—figure supplement 3.

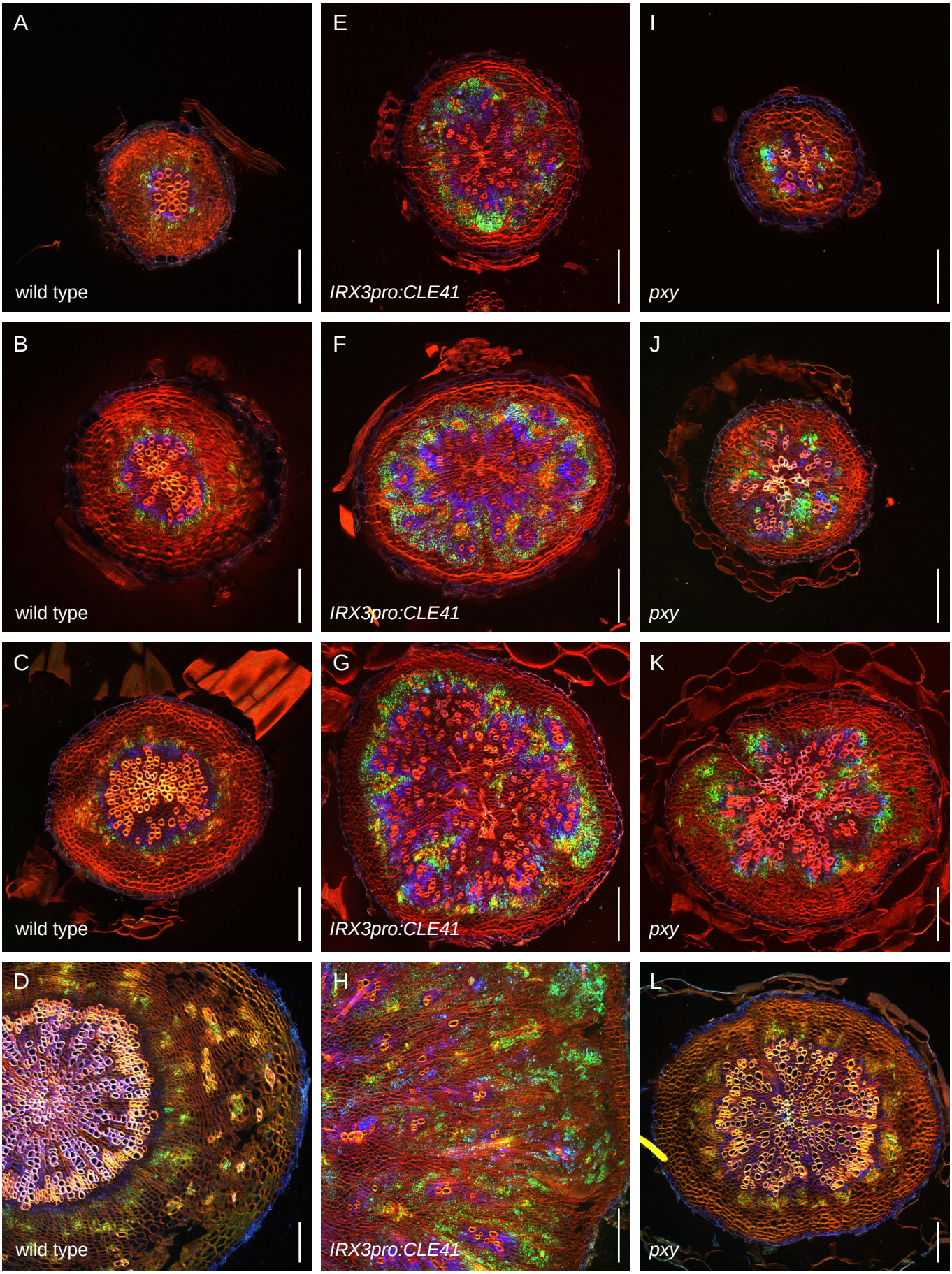

Figure 3—figure supplement 2. Second example revealing the dynamics of *PXYpro:CFP/SMXL5pro:YFP* activities during radial hypocotyl growth in wild type, *IRX3pro:CLE41* and *pxy* plants.
(A-D) *PXYpro:CFP* (blue) and *SMXL5pro:YFP* (green) activities at different stages of wild type hypocotyl development from young (A) to old (D). **(E-H)** *PXYpro:CFP* (blue) and *SMXL5pro:YFP* (green) activities at different stages of hypocotyl development in *IRX3pro:CLE41* plants from young (E) to old (H). **(I-L)** *PXYpro:CFP* (blue) and *SMXL5pro:YFP* (green) activities at different stages of hypocotyl development in *pxy* mutants from young (I) to old (L). Sections are stained by Direct Red 23 (red). Scale bars: 100 µm. A version of this figure for color-blind readers is provided in Figure 3—figure supplement 4.

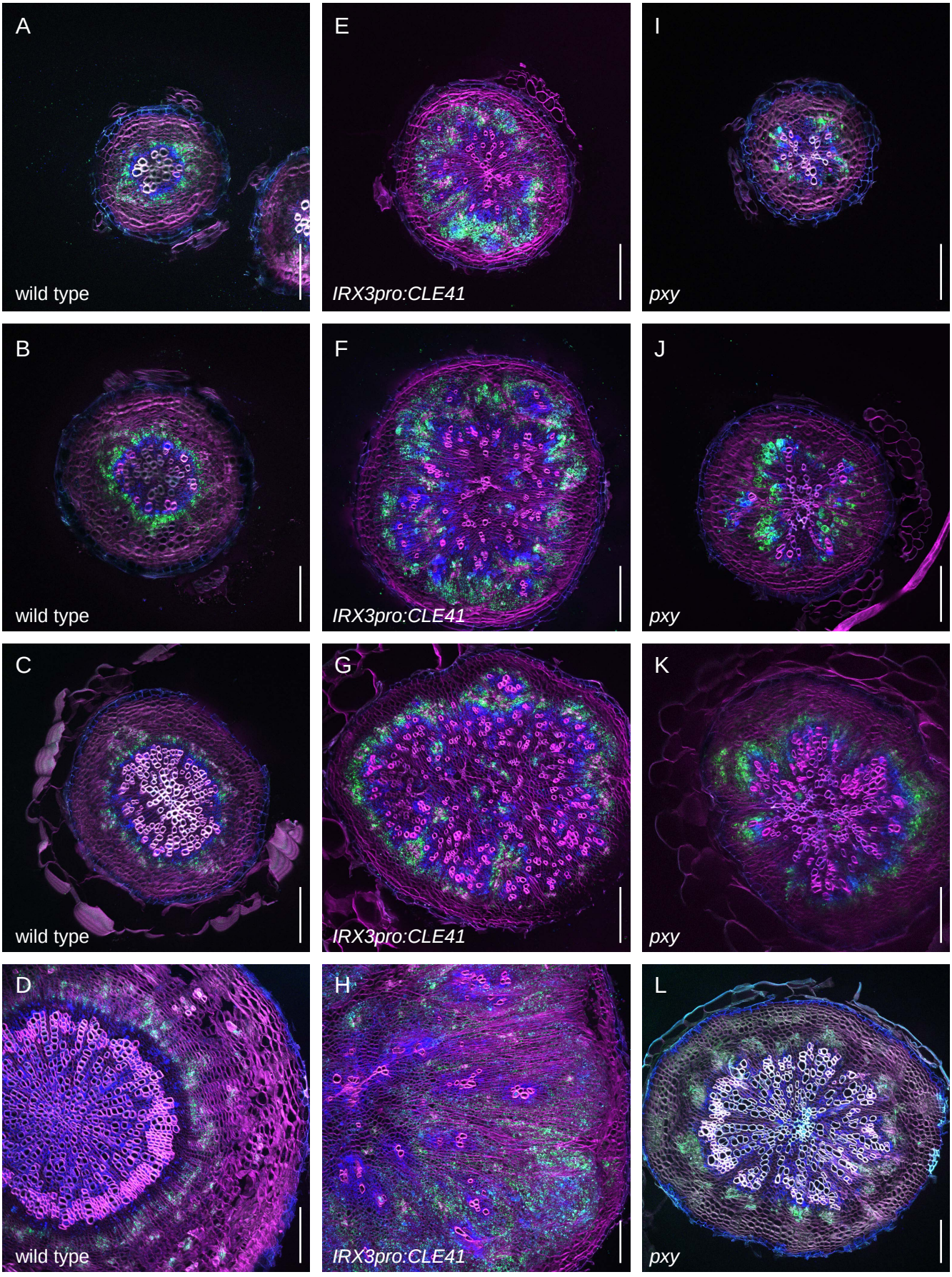

Figure 3—figure supplement 3. First example revealing the dynamics of *PXYpro:CFP/SMXL5pro:YFP* activities during radial hypocotyl growth in wild type, *IRX3pro:CLE41* and *pxy* plants (color-blind mode).
(A-D) *PXYpro:CFP* (blue) and *SMXL5pro:YFP* (green) activities at different stages of wild type hypocotyl development from young (A) to old (D). **(E-H)** *PXYpro:CFP* (blue) and *SMXL5pro:YFP* (green) activities at different stages of hypocotyl development in *IRX3pro:CLE41* plants from young (E) to old (H). **(I-L)** *PXYpro:CFP* (blue) and *SMXL5pro:YFP* (green) activities at different stages of hypocotyl development in *pxy* mutants from young (I) to old (L). Sections are stained by Direct Red 23 (red). Scale bars: 100 µm. Note that pictures D, H and L are also depicted in Figure 2 and Figure 3.

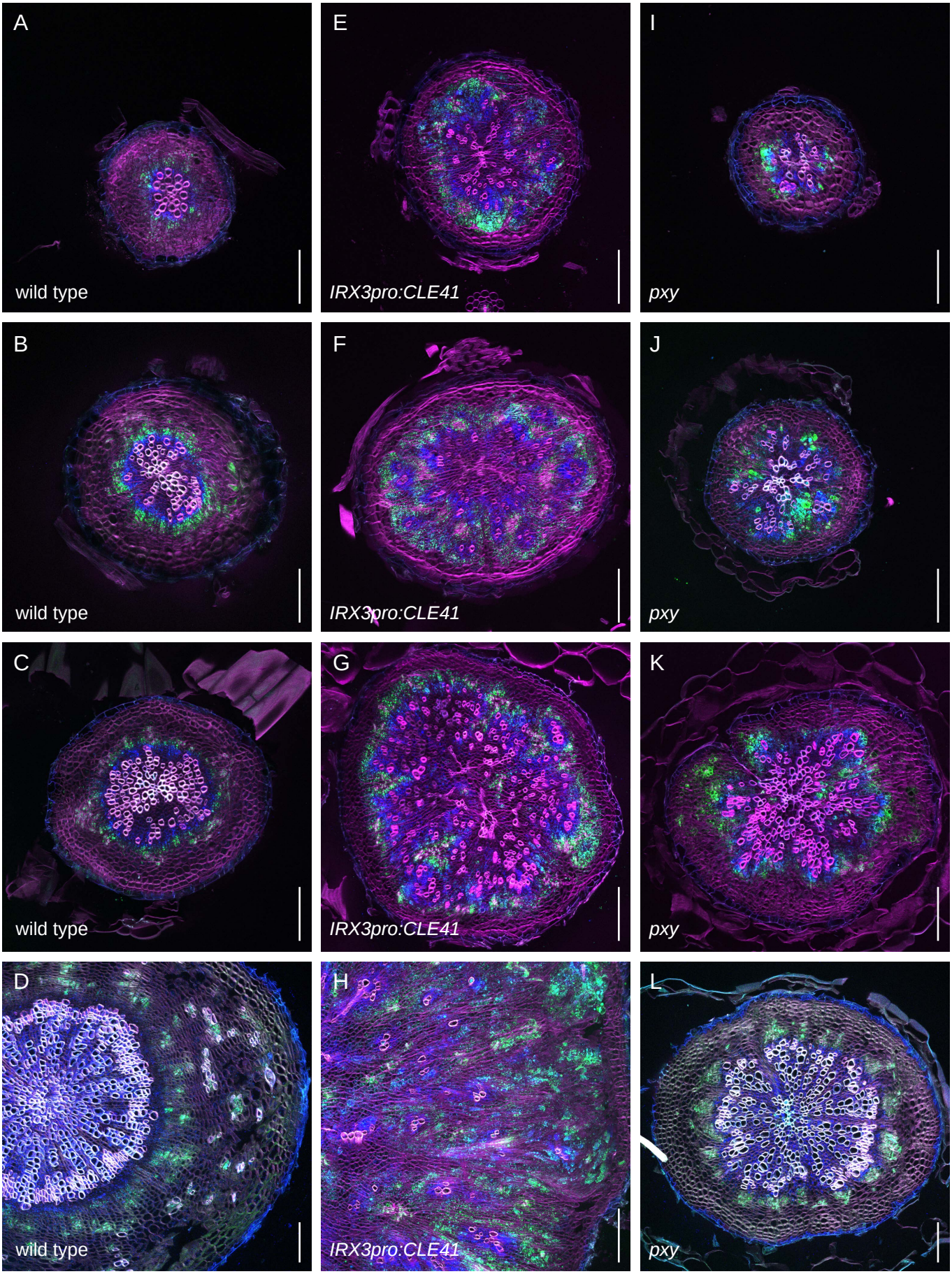

Figure 3—figure supplement 4. Second example revealing the dynamics of *PXYpro:CFP/SMXL5pro:YFP* activities during radial hypocotyl growth in wild type, *IRX3pro:CLE41* and *pxy* plants (color-blind mode).
(A-D) *PXYpro:CFP* (blue) and *SMXL5pro:YFP* (green) activities at different stages of wild type hypocotyl development from young (A) to old (D). **(E-H)** *PXYpro:CFP* (blue) and *SMXL5pro:YFP* (green) activities at different stages of hypocotyl development in *IRX3pro:CLE41* plants from young (E) to old (H). **(I-L)** *PXYpro:CFP* (blue) and *SMXL5pro:YFP* (green) activities at different stages of hypocotyl development in *pxy* mutants from young (I) to old (L). Sections are stained by Direct Red 23 (red). Scale bars: 100 µm.

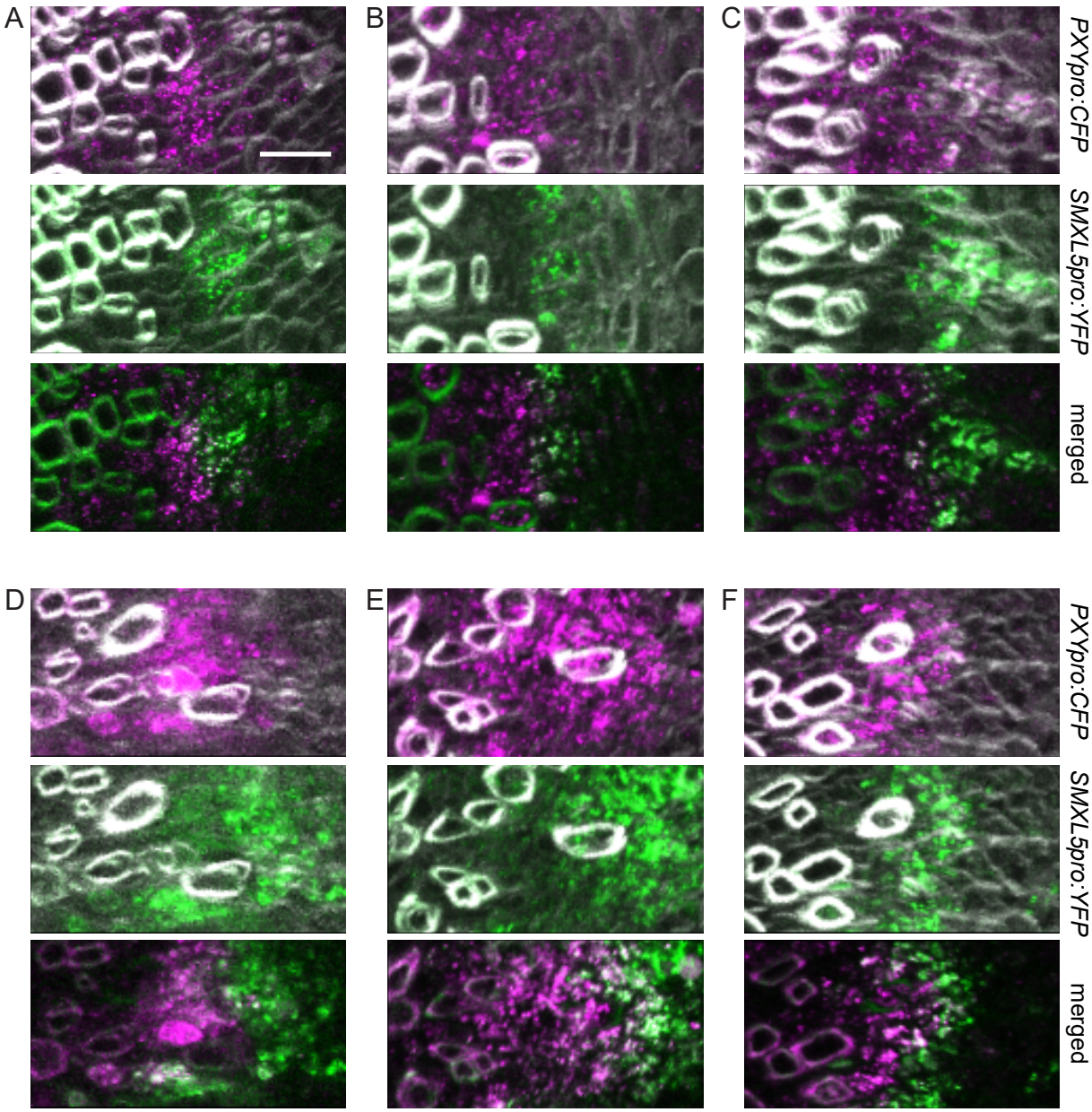

Figure 3—figure supplement 5. Close-up revealing the dynamics of *PXYpro:CFP/SMXL5pro:YFP* activities in hypocotyls in wild type and *pxy* plants.
(A-C) Three examples showing *PXYpro:CFP* (top, bottom, in magenta) and *SMXL5pro:YFP* (middle, bottom, in green) activities in the cambium zone of wild type plants. Scale bar in A: 20 µm. Same magnification in A-F. **(D-F)** Three examples showing *PXYpro:CFP* (top, bottom, in magenta) and *SMXL5pro:YFP* (middle, bottom, in green) activities in the cambium zone of *pxy* mutants. Note that Direct Red 23 staining (in grey) is only shown in top and middle imageds but not in 'merged' images at the bottom. Shown are stages as depicted in Figure 3—figure supplement 1C, K and Figure 3—figure supplement 2C, K.

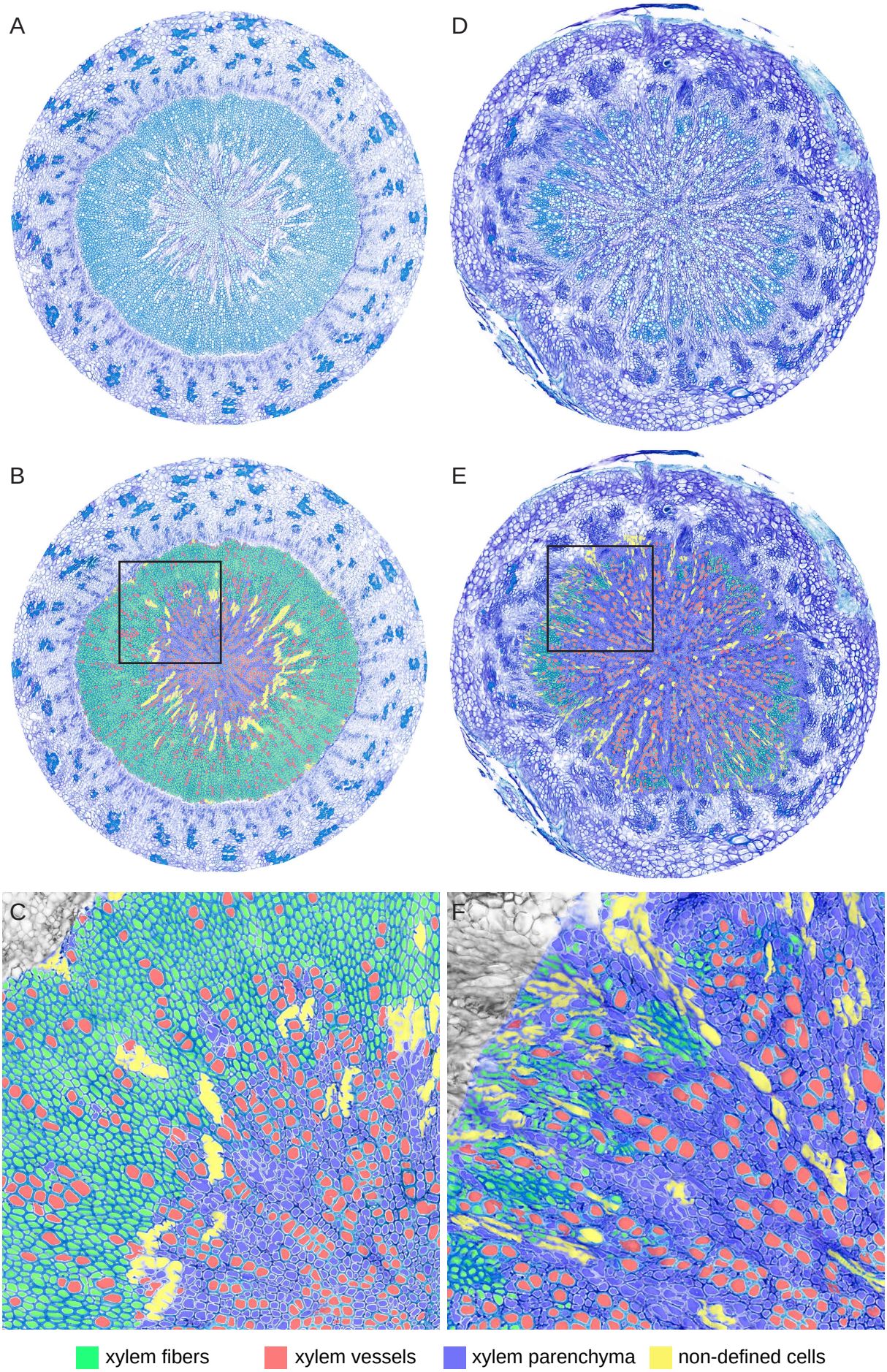

Figure 3—figure supplement 6: Overview and magnifications of sections used for cell type classification shown in Fig. 3.
Original toluidine-stained cross sections (A, D), cross section with cell type-classifications (B, E) and magnifications of regions indicated by black rectangles in B and E (C, F) for wild type (A, B, C) and *pxy* mutants (D, E, F) are shown. Cell type classification was exclusively performed in the xylem area.

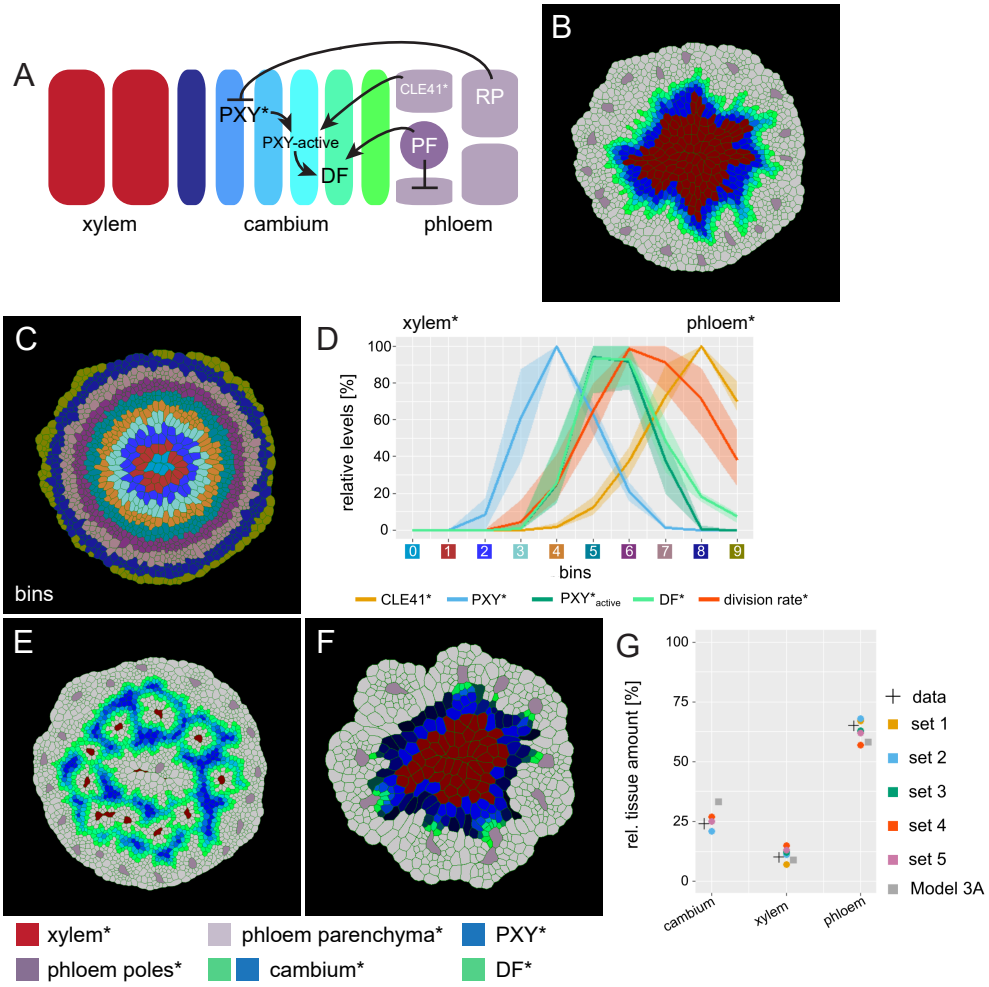

Figure 4. An extended model for simulating genetic perturbations of cambium activity.
(A) Regulatory network proposed based on experimental observations.
(B) Result of the simulation run for Model 3A. This model implements the network interactions described in (A). Color coding at the bottom of Figure 4.
(C) Outline of cell bins for the results of Model 3A, as shown in (B).
(D) Visualization of the relative levels of chemicals* and division rates* in different bins. Bin colors along the x-axis correspond to the bin colors in (C).
(E) Output of Model 3B simulation. Ectopic CLE41* expression was achieved by letting xylem cells* produce CLE41*.
(F) Output of Model 3C. Simulation of the pxy mutant was achieved by removing the stimulation of DF* production by PXY* and hence by removing the effect of PXY* on cell division and cambium* subdomain patterning. Because of the network structure, PXY* can be eliminated from Model 3 without letting the model collapse (Figure 4F) but reproducing the pxy mutant phenotype observed in adult hypocotyls (Figure 4E).
(G) Estimated tissue ratios for five identified parameter sets compared to experimental values ('data') found for wild type (Col-0) hypocotyls 20 days after germination [38] and compared to the final model output before the automated parameter search ('Model 3A') and the implementation of experimentally determined cell wall thickness for xylem* and phloem*.

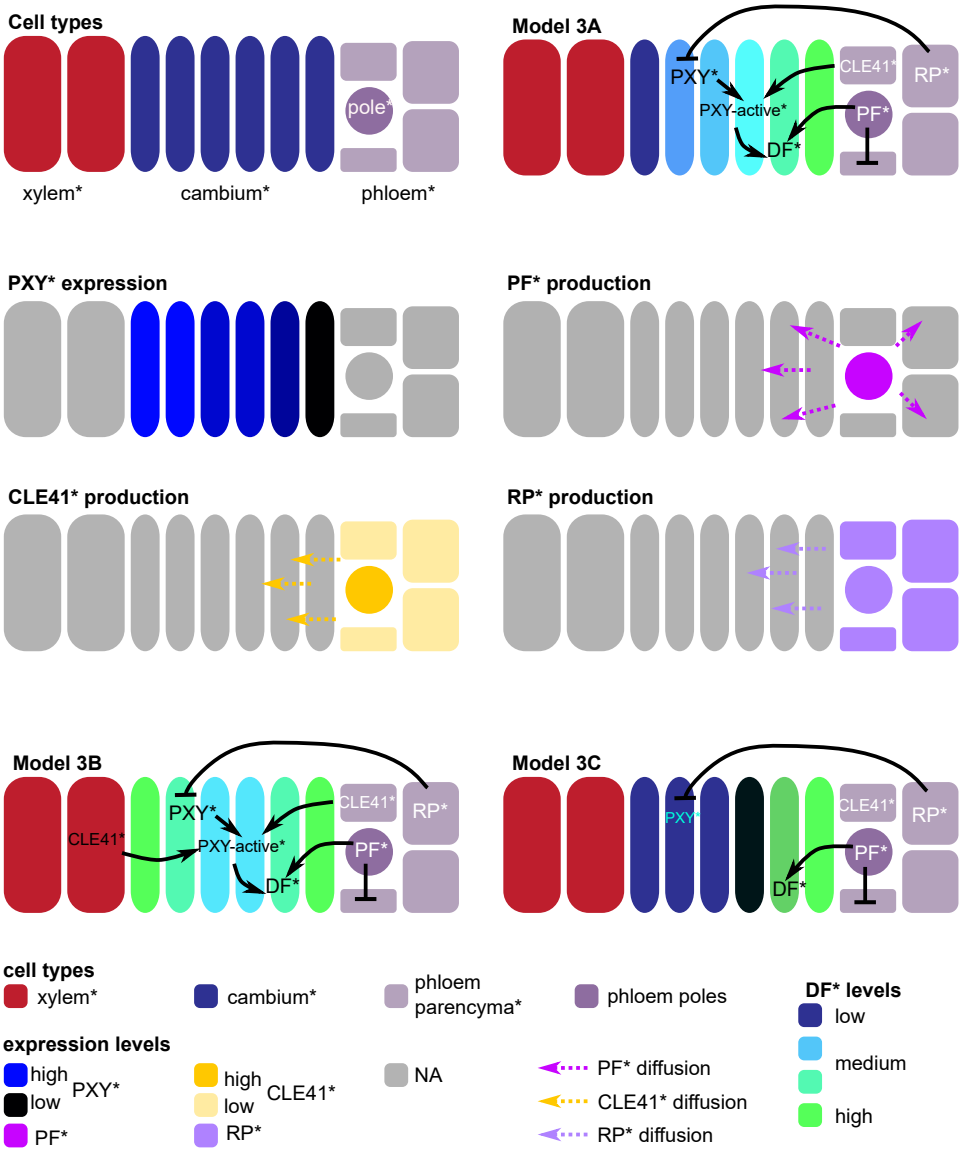

Figure 4—figure supplement 1: Overview of cell types*, regulatory interactions and expression* profiles in Model 3. Schemes include representations for Model 3B and C. Color code shown at the bottom of the figure.

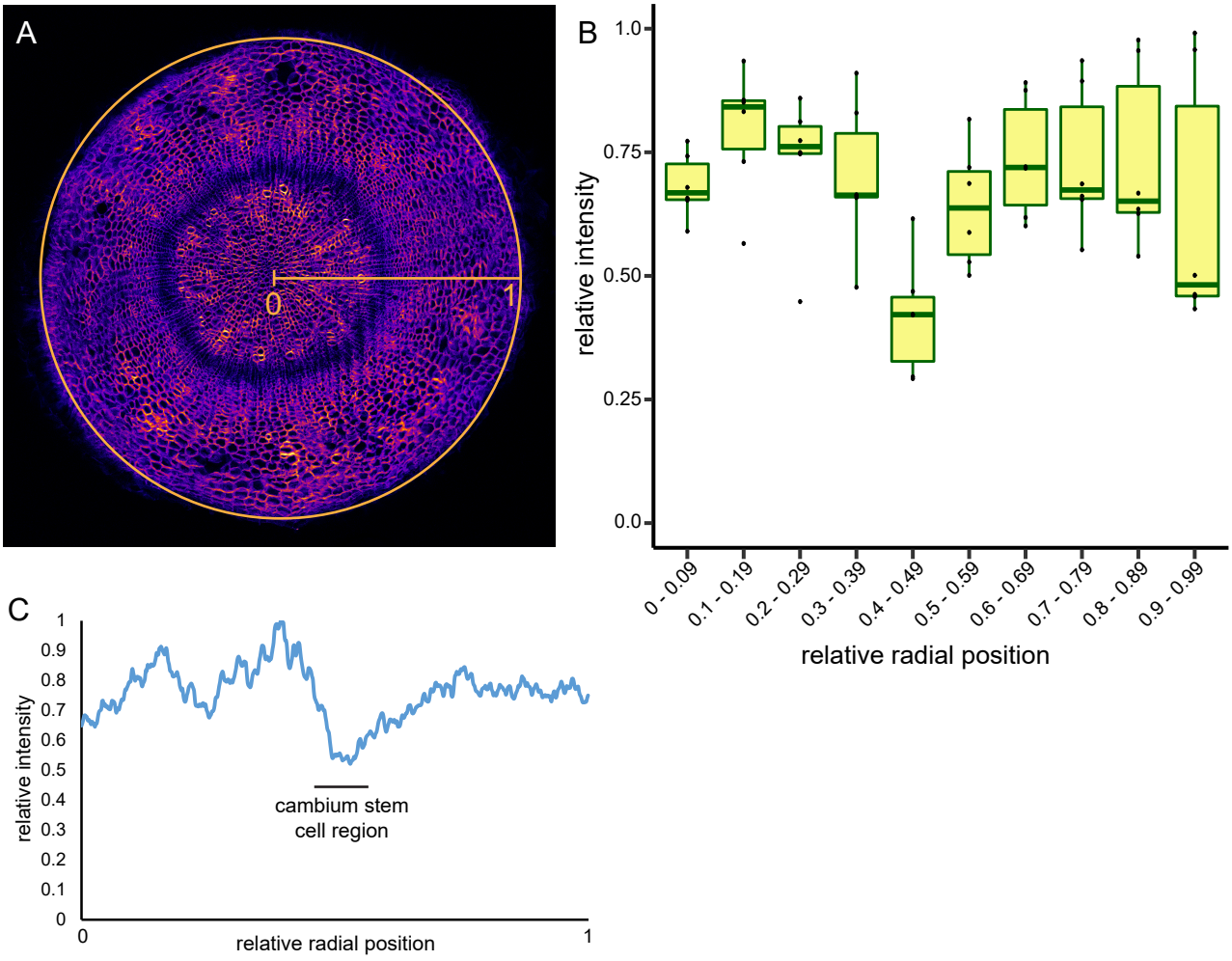

Figure 4—figure supplement 2: Determination of cell wall thickness across the radial sequence of hypocotyl tissues.

(A) Cross section of a 4.5 week-old plant stained by Direct Yellow 96. Radius and circumference used by the 'Radial Profile' function of the Fiji image analysis tool [76] are indicated. Note that the function uses the whole circle area for analysis.

(B) Plot of staining intensities from six Direct Yellow 96-stained cross sections analyzed by the 'Radial Profile' function of Fiji. Staining intensity and radius were normalized to 1 by dividing obtained values by maximum values within respective sample data sets. Intensity profiles were binned in 10 equal parts and the median intensity of single samples was calculated, indicated as dots. The boxplot shows the variation among the samples and the mean of the dataset of each bin.

(C) Average intensity profile of Direct Red 23 staining as shown in Figure 2A from three individual sections determined by the 'Radial Profile' function of Fiji. Staining intensity and radius were normalized to 1 by dividing obtained values by maximum values within respective sample data sets.

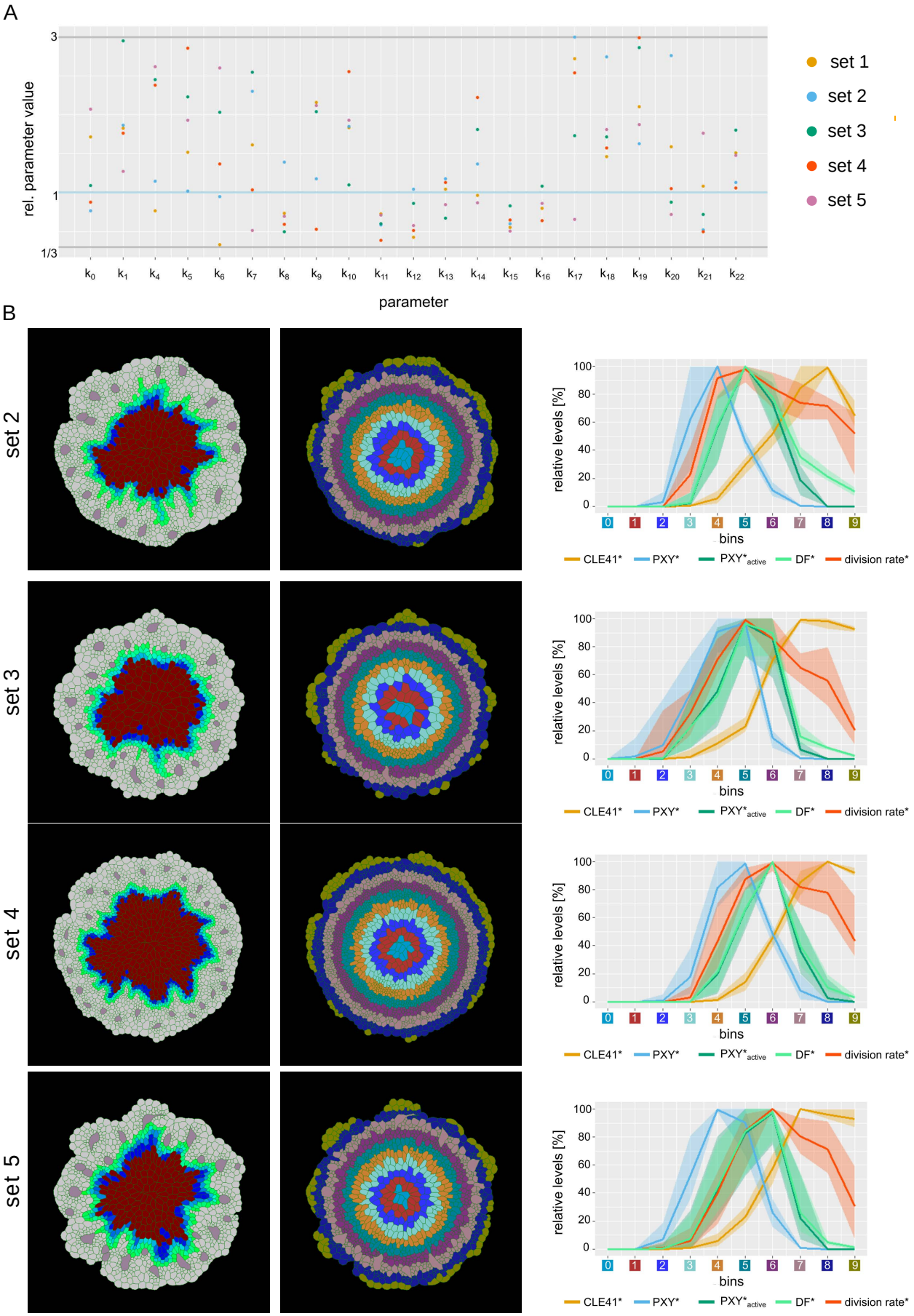

Figure 4—figure supplement 3: Behavior of the different model parameterizations (Model 3D:2-5).
(A) Overview of parameter values of the different parameter sets. Shown are the relative values of the estimated parameter compared to the original parameter values. Horizontal lines indicate the lower (1/3) and upper (3-fold) boundary (grey) as well as the original parameter value (blue).
(B) Behavior of parameter sets 2-5. Shown is the final output of the simulation, the tissue* sorted into bins as well as the average chemical concentration* per bin (for n=10 simulations). The shading represents the range between minimal and maximal values during simulations.

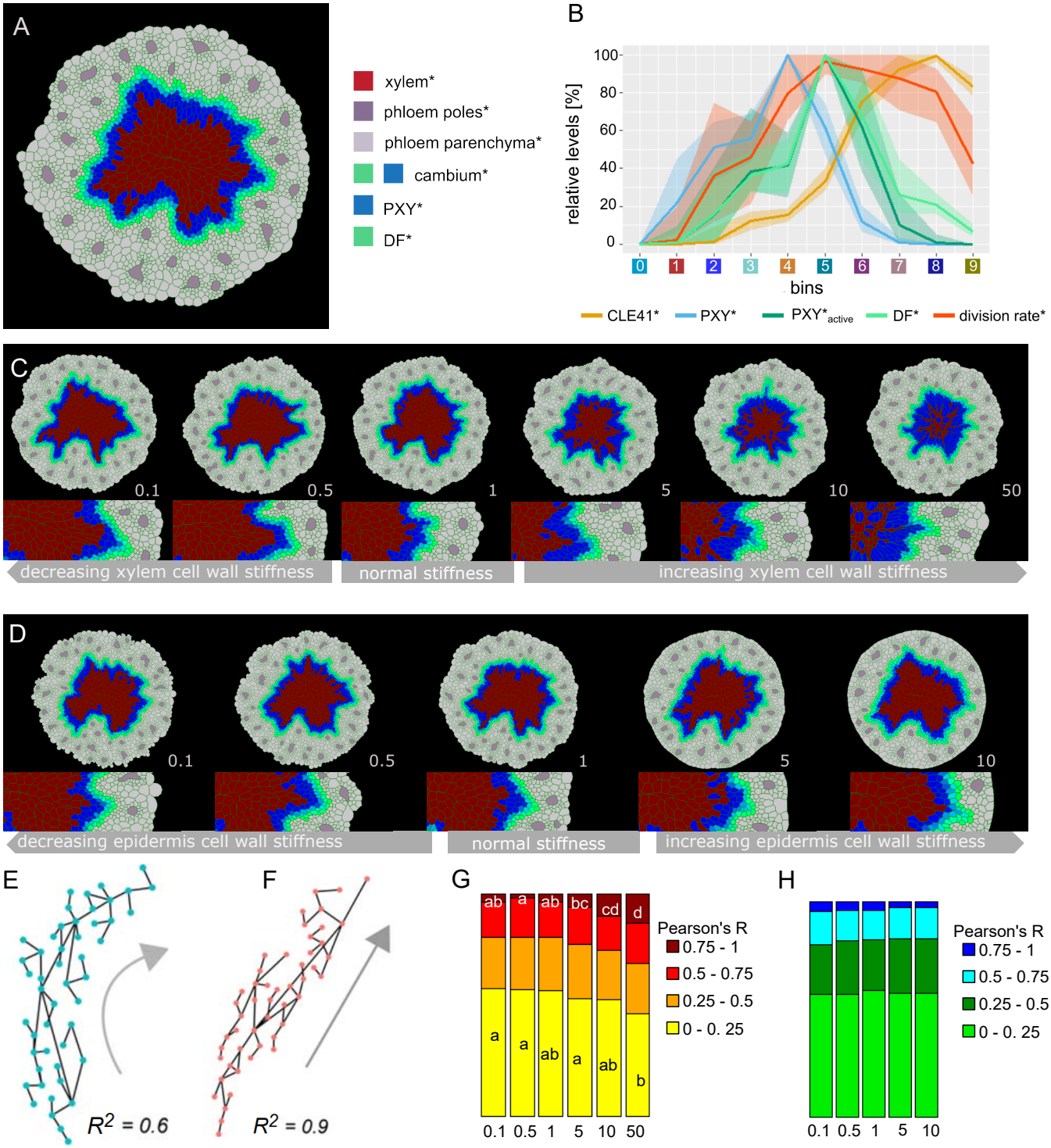

Figure 5. Effect of xylem cell wall stiffness* on the radiality of cambium-derived cell lineages*.
(A) Final output of Model 4 and parameter set 1.
(B) Visualization of the relative levels of chemicals* and division rates* in different bins. Bin colors along the x-axis correspond to the different bins similarly as in Figure 4C.
(C, D) Simulation outputs at increasing values of xylem stiffness* (C) and epidermis stiffness* (D) with the ratio of stiffness* vs. experimentally determined xylem stiffness indicated at the right bottom corner of each example. All the simulations had the same starting conditions and ran for the same amount of simulated time. At the bottom, there is a magnification of the right region shown in the pictures above, respectively.
(E, F) Examples of the relationship between R^2 and the geometry of proliferation trajectories (grey arrows) for two different R^2 values; dots are cell* centroids, lines represent division* events.
(G, H) Fraction of median relative amount of lineages whose R^2 falls within a specific range for ten simulations in each condition (n≥70 lineages per simulation) at different xylem stiffness* (G) and epidermis stiffness* (H) regimes. In case of significant difference among medians, assessed with Kruskal-Wallis (KW significance is $p < 1.01E-5$ for (0, 0.25) interval and $p < 1.04E-7$ for the (0.75,1) interval), the pairwise difference between medians was tested post hoc applying the Dunn test. The post hoc results are reported in each box as letters; medians sharing the same letter or do not display a letter at all do not differ significantly.

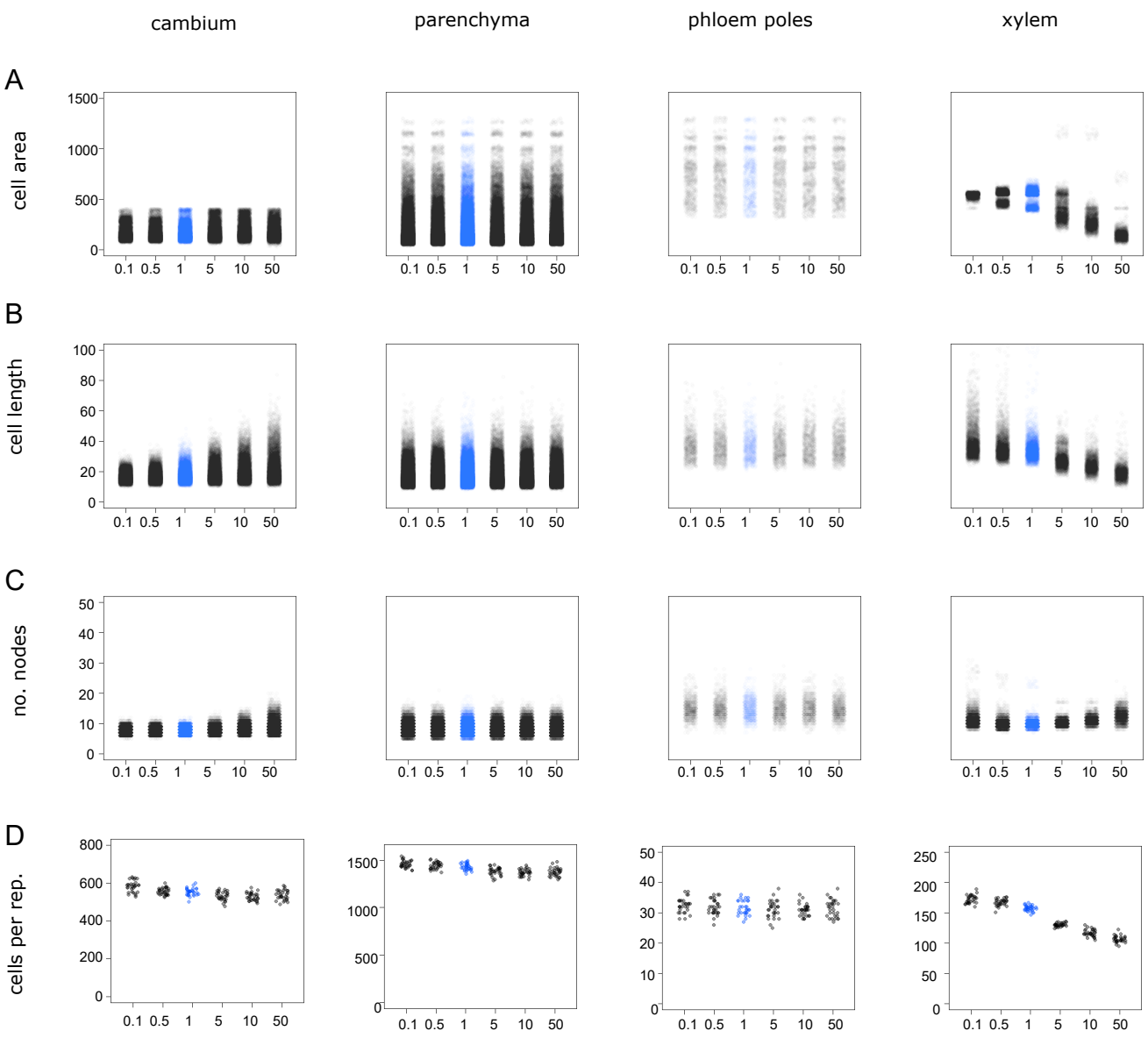

Figure 5—figure supplement 1: Distribution of cell* properties under different xylem 'stiffness' regimes
A) Cell* size in arbitrary units
B) Major axis lengths of cells* in arbitrary units
C) Numbers of nodes (vertexes) per cell*
D) Numbers of cells*
among cell types and stiffness values for n = 30 simulations under each stiffness regime. The blue color highlights the simulation at the experimentally determined stiffness value. The x-axis indicates values of xylem stiffness as the ratio of xylem stiffness* vs. experimentally determined stiffness. A slight horizontal displacement of points has been added to enhance visualization. Values for individual cells* found in all 30 simulations are displayed in A-C, whereas numbers of cells* in each cell type* for each one of the 30 simulations are shown in D.

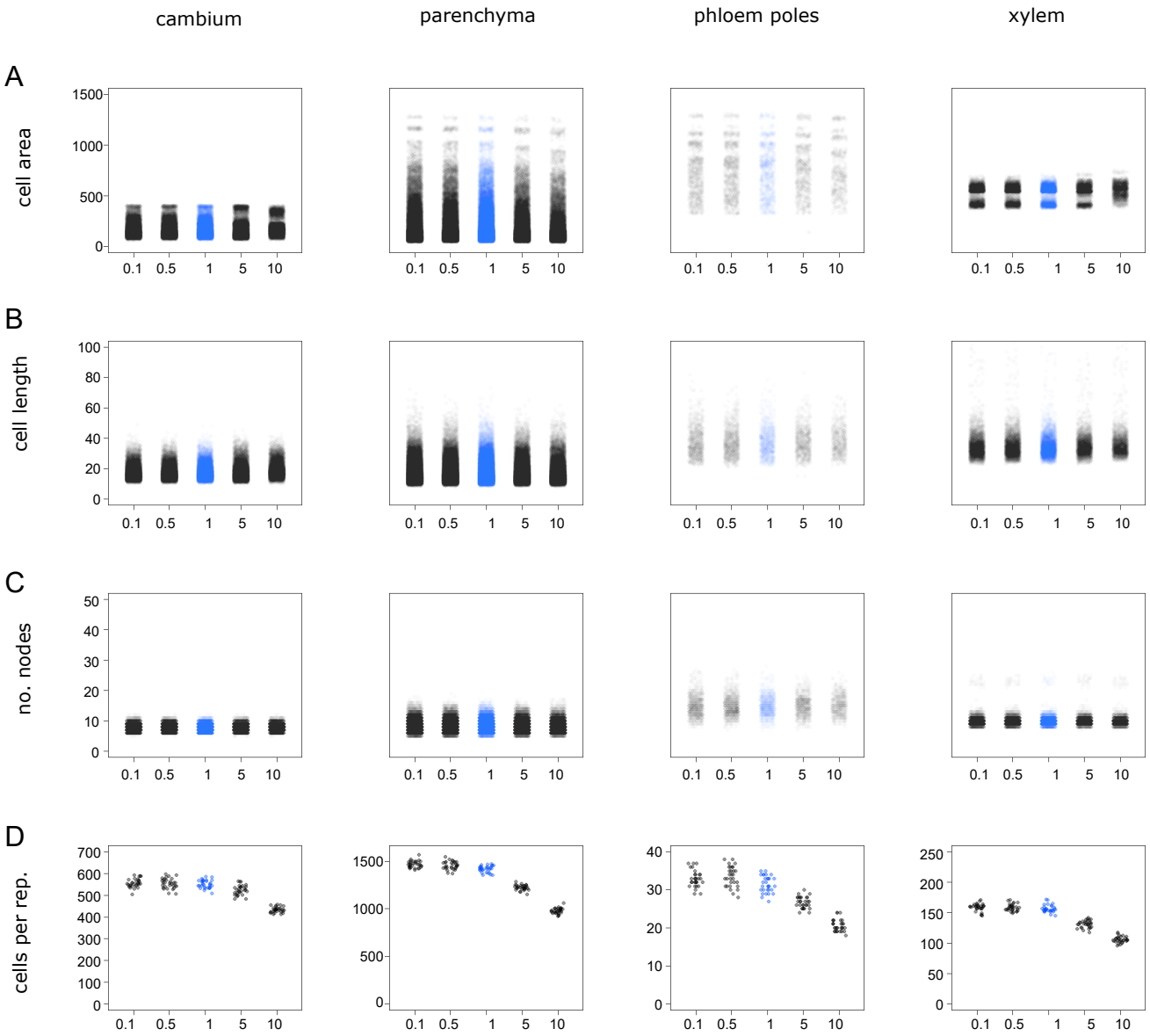

Figure 5—figure supplement 2: Distribution of cell* properties under different tissue boundary (=epidermis*) 'stiffness' regimes
(A) Cell* size in arbitrary units
(B) Major axis lengths of cells* in arbitrary units
(C) Numbers of nodes (vertexes) per cell*
(D) Number of cells*
among cell types and stiffness values for n = 30 simulations under each stiffness regime. The blue color highlights the simulation running at normal thickness level; the x-axis indicates values of the relative perimeter thickness as the fold-change compared to the standard parameters. A slight horizontal displacement of points has been added to enhance visualization. Values for individual cells* found in all 30 simulations are displayed in A-C, whereas numbers of cells* in each cell type* for each one of the 30 simulations are shown in D.

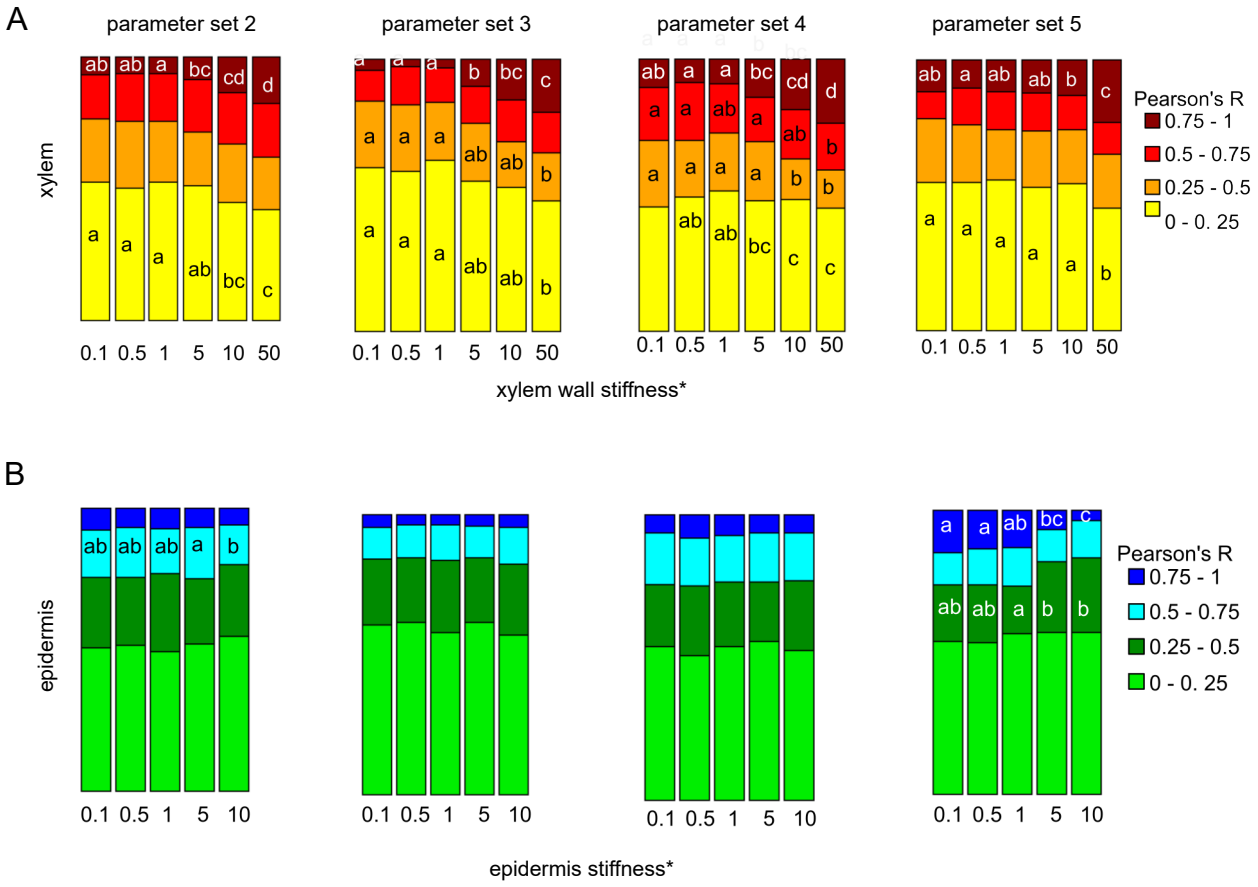

Figure 5—figure supplement 3: Fraction of median relative amount of cell lineages for parameter sets 2-5.
(A) With increasing xylem* 'stiffness'
(B) With increasing epidermis* 'stiffness'

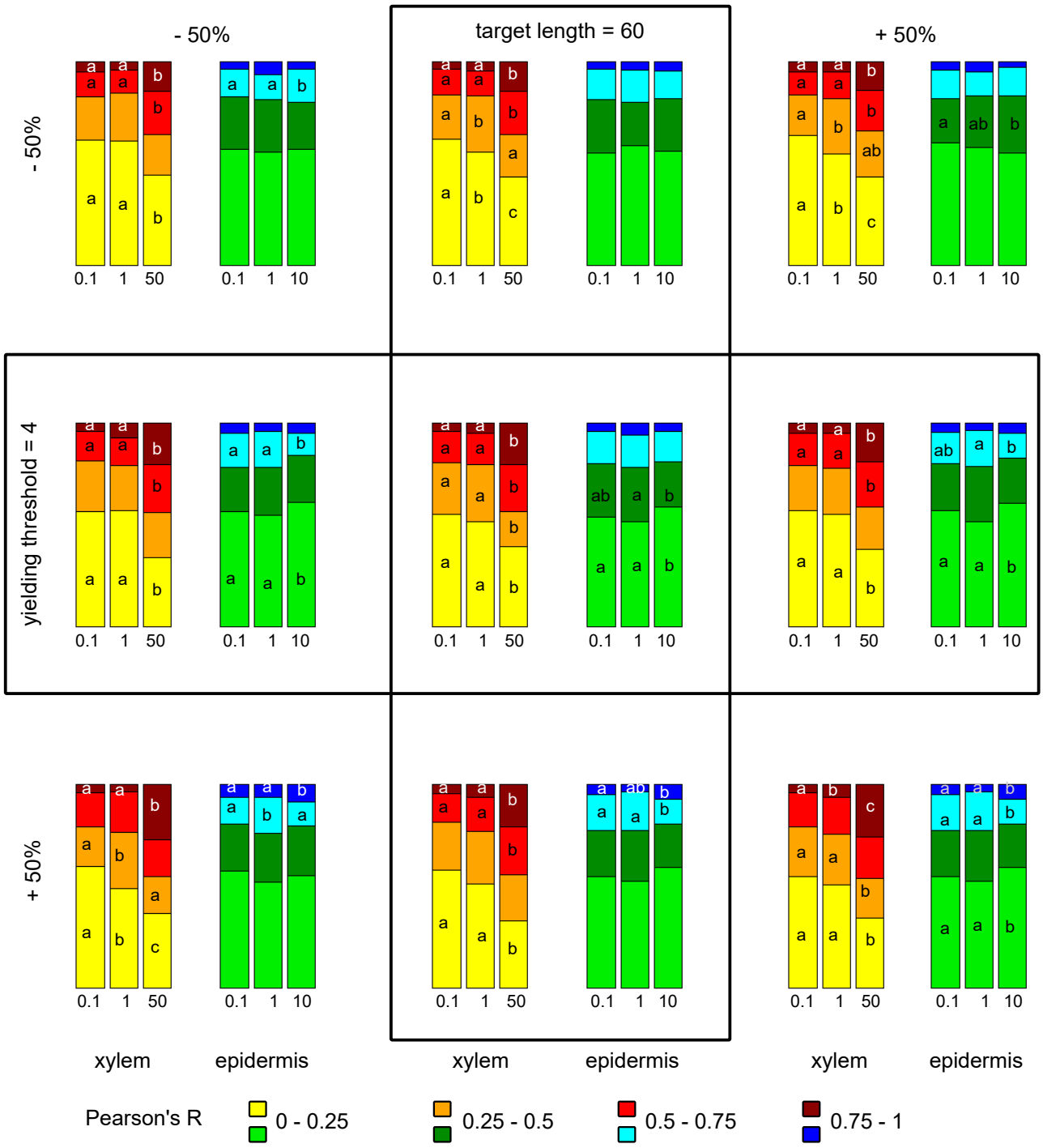

Figure 5—figure supplement 4: Fraction of median relative amount of cell lineages at different parameters governing cell wall* dynamics. The model parameters cell walls' target length and yielding threshold were varied by +/-50% and the behavior at different cell wall stiffness values simulated. The statistical analysis was done as described before for Fig. 5 for n=10 simulations each and n≥70 cell lineages per simulation.

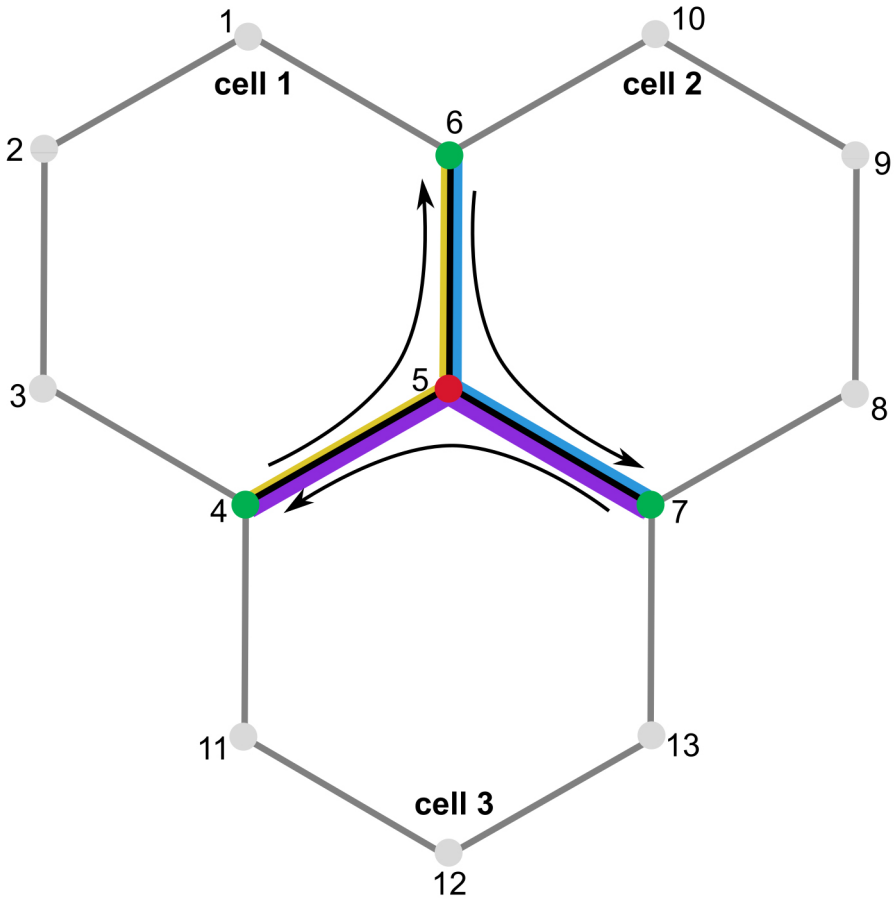

Appendix-figure 1 - Cell wall calculations during node movement. Node 5 is moved to a new position. During calculations the change in wall elements between nodes 5 and 6, 5 and 7 as well as 5 and 4 is considered. The cell specific stability of the wall elements is indicated by the thickness of the colored lines – yellow for cell 1, blue for cell 2 and purple for cell 3.